

effect, if confirmed, would constitute another example of TCEE.

4.2.2 Autoionization and Auger Emission

If a target atom is in an excited state with an energy above the ionization limit, it can make a spontaneous transition to a continuum state resulting in the emission of an electron of a well-defined energy. This mechanism, known as autoionization, can result from at least two kinds of excitation. Atoms (other than one-electron atoms) can be doubly excited in collisions. Helium, *e.g.*, may be excited from its $1s^2$ ground state to a $2s2p$ state. The other kind of autoionizing state results from a vacancy in an inner shell. This may be caused either by raising an inner-shell electron into a vacancy in an outer shell or by removing it entirely. The subsequent process of filling the inner-shell vacancy is called an *Auger* transition if an outer-shell electron is involved, or a *Coster-Kronig* transition if an electron from the same shell but different subshell fills the vacancy. Provided that certain selection rules are satisfied, autoionization and Auger electrons are emitted rapidly. Typical lifetimes are about 10^{-13} to 10^{-15} s.

The initial ionization leading to an inner-shell vacancy takes place in a manner similar to that for outer-shell ionization and the spectrum of ejected electrons is continuous. However, the ensuing autoionization process, resulting in a second electron being ejected, yields instead a discrete spectrum due to the transition between well-defined initial and final states.

The discrete spectrum which is superimposed on the continuum resulting from the other mechanisms does not usually contribute much to the TICS and is ignored in most theoretical treatments and in the semi-empirical models which describe the secondary electron spectra. However, it does contribute strongly in certain regions of the spectrum and becomes more important for very low energy collisions and for heavier projectiles. Reviews dealing with high-resolution spectroscopy of Auger electrons have been given by Mehlhorn (1985) and by Stolterfoht (1987).

4.2.3 Electron Promotion

Early studies of inelastic energy losses in $\text{Ar}^+ + \text{Ar}$ collisions (*e.g.*, Afrosimov *et al.*, 1965; Kessel and Everhart, 1966) revealed unexpectedly large cross sections for the production of L-shell vacancies, resulting in the emission of Auger electrons. This work was reviewed by Kessel and Fastrup (1973).

If the collision takes place at a small impact parameter and the projectile speed is smaller than the orbital speed of the electron in the target atom, it is appropriate to consider a temporary molecule formed during the collision (Fano and Lichten, 1965). As the collision proceeds and the projectile approaches the

target, the energies of the molecular states change. Sometimes the energy levels cross and an electron may end up on a higher level after the collision is over. This mechanism, known as *electron promotion*, is very efficient in producing inner-shell vacancies. It is an important mechanism when two heavy atoms collide but contributes little to the spectrum of electrons from proton and other light ion collisions. A mathematical treatment of electron promotion for proton impact was given in Rudd (1979).

4.2.4 Multiple Ionization

Measurements of charge states of residual ions from collisions show clear evidence of cases where more than one electron is removed in a single collision. DuBois and Manson (1987) describe several ways that this can happen. One is through Auger emission following the creation of an initial inner-shell vacancy as discussed in Section 4.2.2. An Auger cascade following the initial electron ejection from an inner shell of a heavy atom can produce a highly charged ion. In a large enough atom, an Auger cascade can result in nearly complete stripping of the outer shell.

Another mechanism called *transfer ionization* is the simultaneous ejection and capture of electrons. See, *e.g.*, Niehaus (1980) and Salzborn and Müller (1986). If the recombination energy of the projectile is greater than the binding energy of the target, the cross section for this process is large and nearly constant as the primary energy approaches zero.

Another possible way to eject more than one electron from an atom is by a double interaction. A single ion passing through an atom may interact successively with two electrons and eject both. Alternatively, the ion may eject one electron; however, if energetic enough, that electron may interact with a second electron before leaving the atom (DuBois and Manson, 1987).

Multiple ionization is more important for heavy targets (with many electrons) than for lighter ones. For example, for 1-MeV protons only about 0.7% of all ionizing collisions with helium result in more than one electron being ejected, while for proton collisions with argon, over 4% of the collisions yield double ionization, 1% result in triple ionization, and about 0.2% yield Ar^{4+} ions.

For proton impact, the contribution of multiple ionization to the TICS is small but its relative importance is greater at larger electron emission energies as shown in Figure 4.5. These data are for situations where neither electron capture nor inner-shell ionization processes are significant; they are for multiple outer-shell ionization only. The data clearly demonstrate that multiple ionization contributes significantly to energetic electron emission, an effect which

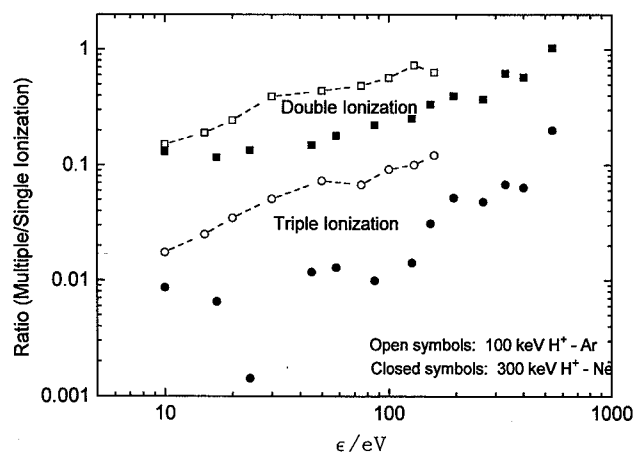


Fig. 4.5. Ratio of multiple to single ionization cross sections as a function of the energy of the ionized electron. \circ, \square , 100 keV H^+ - Ar data of Chung (1993); \bullet, \blacksquare , 300 keV H^+ - Ne data of Hippler *et al.* (1984).

has not been considered in existing energy deposition models.

Multiple outer-shell ionization resulting from independent interactions between the projectile and the target electrons dominates at lower impact energies (DuBois and Toburen, 1988). In this case, the probability, P_n , of ionizing n electrons in an outer shell containing m electrons can be calculated by assuming a binomial distribution (Hansteen and Mosebekk, 1972; McGuire, 1992):

$$P_n = \binom{m}{n} P^n (1 - P)^{m-n}, \quad (4.1)$$

where P is the probability of ionizing a single electron. However, other processes, *e.g.*, inner-shell ionization leading to Auger electron emission, also result in multiple target ionization and these processes will influence the total and differential ionization cross sections differently.

4.2.5 Mechanisms Involving Projectile Electrons

The spectrum of electrons from collisions by dressed projectiles may be significantly affected by the electrons carried by the projectile. The role of projectile electrons was first studied by Bates and Griffing (1953), who distinguished the two characteristic cases. In the first part of the Bates-Griffing scattering mechanism, the electron on the incident particle is assumed to remain in its ground state during the interaction with the active target electron.

The second part of this scattering mechanism comes into play as the incident electron is removed from its ground state. The ejected electron interacts with the target electron on equal terms. The resulting two-electron event is referred to as a *dielectronic process* (Stolterfoht, 1991).

Significant projectile ionization also occurs through the interaction of the target nucleus with the projectile electrons. In this case, the collision system may be considered as being reversed with the target taking the role of the projectile and vice versa.

Bound projectile electrons also influence the electron emission by introducing "diffraction effects" because of the screened-Coulomb fields in which the emitted electrons travel. These effects are particularly important for close collisions involving heavy, dressed ions and hence are observed as deviations from the expected behavior of the binary encounter emission.

4.3 Experimental Methods

4.3.1 Total Ionization Cross Sections

The condenser-plate or transverse-field method described in Section 3.3.1 has been used in most measurements of TICSs for ion impact. Other methods include the integration of DDCSs (see following Section) and measurements of the energy loss of projectiles. For a fuller discussion of the measurement of TICSs, see the review by Rudd *et al.* (1985a).

4.3.2 Angular and Energy Distributions

Information about the energy spectrum of secondary electrons as well as their angular distribution is contained in the doubly differential cross section (DDCS). This is measured in much the same manner as for electron impact as described in Section 3.6.1 and the relation between the SDCS, $\sigma(\epsilon)$, and the TICS, σ_i , is given in Eq. 1.5. For ion impact there is no well-defined upper limit to the electron energy, except, of course, the projectile energy itself which is usually so much higher than the energy of most electrons that ϵ_{\max} may usually be taken to be infinity.

The most common method of measuring the DDCS uses a rotatable electrostatic deflection-type analyzer placed at various angles relative to the beam. The analyzer-detector system views electrons from a short section of the beam at the collision center. By proper choice of slit sizes and other dimensions, a narrow range of energies of electrons is passed by the analyzer to the detector which is operated in the pulse counting mode.

A schematic diagram of a typical apparatus for measuring DDCSs is shown in Figure 4.6. Projectile ions are formed in an ion source by ionization of an appropriate gas, accelerated to the desired energy, passed through a deflection magnet to eliminate impurity ions, and directed into the target gas at the collision center. Single collision conditions are maintained in which the density of the target gas is low enough that a large fraction of the ions pass through the gas without making collisions. They are collected

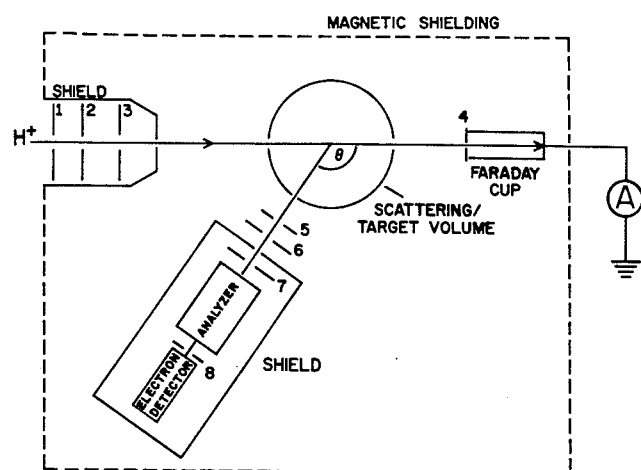


Fig. 4.6. Schematic diagram of apparatus used to measure DDCSs for electron ejection. The beam entering from the left is collimated by apertures 1 and 2. Aperture 3 is a secondary electron suppressor. The beam traverses the collision region and enters the Faraday cup with suppressor aperture 4. Secondary electrons ejected at an angle θ are collimated by apertures 5 and 6, preaccelerated by 7, and enter the electrostatic analyzer. Electrons with energies within the bandpass of the analyzer leave through slit 8 and are detected (from Rudd *et al.*, 1992).

in a Faraday cup which has been biased to prevent secondary electrons produced in the cup from escaping.

In some experiments a gas cell is used to contain the target gas at a low pressure (typically 10^{-5} to 10^{-3} torr). Small apertures allow the beam to pass through and the electrons to exit to the analyzer. Since the flow of gas out through these apertures is relatively slow, the target is essentially a static gas the density of which can be determined by measurements of the pressure and temperature. With a static gas the effective beam path viewed by the analyzer/detector system is easily calculated from its slit geometry and varies as $1/\sin\theta$ as the angle is varied.

In other experimental arrangements, the target gas is introduced through a capillary tube or capillary array which produces a diffuse gas beam. This crosses the ion beam at the collision center and enters the inlet of a high speed vacuum pump. This method of introducing the target gas has the advantage of confining it mostly to the collision region. However, it is difficult to determine the effective beam path length L viewed by the analyzer since the density of the target gas varies along the beam. Furthermore, the product $L\Delta\Omega$ varies in an unknown way as the angle is changed. Therefore, when this type of target is used, the data are usually normalized at each angle to measurements made with a static gas.

A major problem in the measurement of cross sections for low energy electron emission (below about 15 eV) is the effect that stray electric and magnetic fields have on the trajectories of slow electrons. The magnetic field of the earth is often neutral-

ized by the use of Helmholtz coils around the apparatus or by magnetic shielding or both. Non-magnetic materials must be used in constructing the parts of the apparatus within the coils or shield and all electrical leads carrying potentials must also be shielded. Stray electric fields may arise when electrons and ions from the collision region are deposited on insulating surfaces. A thin film of oil on a metal surface may collect enough charge to affect the motion of the electrons to be detected. Toburen and Wilson (1975) resolved some of these difficulties by developing a time-of-flight (TOF) technique to replace the electrostatic analyzers generally used. Their system involved a relatively short path length between the collision center and the detector to minimize the effect of stray fields. However, the data obtained by the TOF system are relative and have to be normalized to absolute data taken with an electrostatic analyzer.

The major sources of uncertainty in the measurement of absolute values of DDCSs are in the measurement of pressure (typically 5–10%) and in the determination of the detector efficiency (also 5–10%). Smaller errors are due to uncertainties in geometrical quantities, errors in integration of the primary beam, and dead time losses in the counter. Added in quadrature, this results in a typical overall uncertainty of 15%. Added to this "base" uncertainty, however, there may be systematic errors. Chief among these are the failure to analyze and detect all low energy electrons, as discussed above. Another problem inherent in electron measurements results from the fact that low energy secondary electrons are generated in large quantities from any surfaces struck by beam particles. If these are not properly suppressed, a spuriously high count of low energy electrons can result. Finally, at a sufficiently high electron energy, the cross sections always decrease to the point where too few counts are recorded to yield statistically meaningful results. This is especially troublesome if there are sources of random background noise pulses.

4.3.3 Energy Spectra

The SDSCS, $\sigma(\epsilon)$, describes the energy spectrum of all secondary electrons regardless of the direction of ejection. The main method used to determine this quantity is the integration of the DDCS over angle using Eq. 1.4. The integration may be done numerically from the data if cross sections over a sufficient range of angles are available. Data at the extreme forward and backward angles are difficult to measure, but fortunately are not as important since the $\sin\theta$ factor at those angles is small. Alternatively, the data may be fitted by a mathematical expression and integrated analytically.

Direct measurements have also been made of the SDSCS by the method of ion energy-loss spectroscopy.

In this method, the ion beam is energy-analyzed after traversing a known length of target gas. Those ions which have lost an energy greater than the ionization potential of the target are assumed to have caused ionization. The SDCS is calculated from the fraction of the beam which has undergone the energy loss corresponding to the various secondary electron kinetic energies. There are, however, other processes such as dissociation and excitation which cause energy losses, and a careful measurement must take account of this fact. This method, which was pioneered by Park and Schowengerdt (1969a; 1969b), requires an ion source with a very small energy spread. A diagram of this apparatus is given in Figure 4.7. Ions from the accelerator pass through the target gas in the collision chamber at ground potential and are then magnetically analyzed, decelerated to a selected energy (typically 2 keV), and analyzed by an electrostatic analyzer. The same power supply is used for both acceleration and deceleration so that any voltage variations do not affect the energy of the decelerated ions. Resolutions of 1 to 2 eV were obtained at energies up to 200 keV. A sweep of the energy-loss spectrum with and without target gas yields the cross section as a function of the energy loss if the pressure-path length product is known. A review of this method was given by Park (1983).

4.4 Theoretical Methods

This section expands on the material in Section 2 for those theoretical methods of calculating ionization cross sections by ion impact. Useful reviews of this subject have been written by Rudd and Gregoire (1969); Rudd and Macek (1972); Ogurtsov (1972);

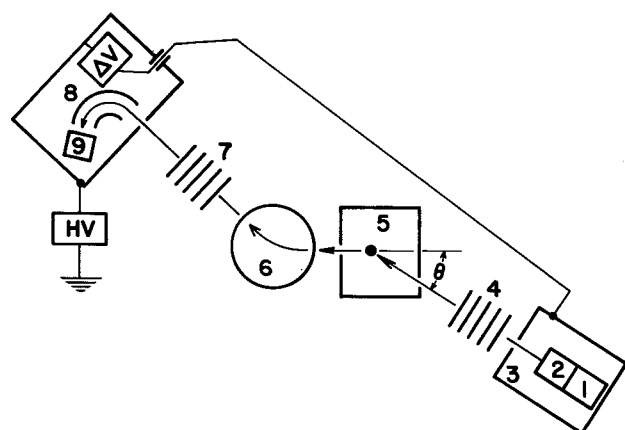


Fig. 4.7. Schematic diagram of ion energy-loss spectrometer described by Park *et al.* (1977). 1, ion source; 2, Wien filter for mass selection; 3, accelerator high-voltage terminal; 4, accelerator column; 5, target center, about which the entire accelerator assembly can rotate; 6, analyzing magnet; 7, decelerator column; 8, decelerator high-voltage terminal containing electrostatic analyzer and ΔV voltage supply; 9, ion detector. The ΔV supply is varied to take the electron-loss spectrum (from Rudd *et al.*, 1992).

Massey and Gilbody (1974); Manson *et al.* (1975); Stolterfoht (1978); and Briggs and Macek (1991).

4.4.1 Binary Encounter Approximation (BEA)

For impact by bare ions of charge Z_1 the Rutherford equation (Eq. 2.3) may be used where the energy transfer Q is related to the secondary electron energy ϵ by $Q = \epsilon + B$, where B is the binding energy. Because of its simplicity, the Rutherford equation, with a cutoff at an energy $\epsilon = 4T$, is often used in radiological work. However, this yields rather poor results as shown in Figure 4.8, where the ratio $Y(\epsilon, T) = \sigma(\epsilon)/\sigma_{\text{Ruth}}(\epsilon)$ is plotted for proton ionization of helium. If the Rutherford equation gave an accurate description, the graph should be a constant at $Y = 2$ since $Z_1 = 2$ for helium, but there are clearly large deviations. Figure 4.9 illustrates the same point.

Much more accurate descriptions are available. Thomas (1927) and Gryzinski (1959; 1965) took account of the initial motion of the electron in the target; this correction makes a pronounced difference in the result. For ion collisions there is a critical secondary energy above which momentum and energy considerations restrict the range of emission angles. This results in a different form of the equation for the two regions. The BEA equation was derived in terms of momentum transfer in a particularly simple way by Vriens (1967) and may be written

$$\sigma(Q) = \sigma_R(Q) \left(1 + \frac{4U}{3Q} \right), \quad \text{for } B \leq Q \leq Q_-, \quad (4.2)$$

and

$$\sigma(Q) = \sigma_R(Q) \frac{U}{Q} \left[\frac{4}{3} \left(\frac{T}{U} \right)^{3/2} - \frac{1}{6} \left[\left(\frac{Q}{U} + 1 \right)^{1/2} - 1 \right]^3 \right], \quad (4.3)$$

for $Q_- \leq Q \leq Q_+$,

where $Q_{\pm} = 4T \pm 4(TU)^{1/2}$, U is the initial orbital kinetic energy of the target electron discussed in Section 2.5.1, and $\sigma_R(Q)$ is the Rutherford cross section (Eq. 2.3).

These equations assume a unique energy of the target electron given by U . Although reasonably good values of singly differential cross sections can be obtained from Eqs. 4.2 and 4.3, there are two flaws in the result. First, there is a discontinuity in the slope of the spectrum at $Q = Q_-$ and second, the cross section drops to zero at $Q = Q_+$. These defects can be corrected by using a more realistic initial electron energy distribution. Rudd *et al.* (1971) incorporated the Fock quantum mechanical hydrogenic distribution of electrons into this BEA equation. The resulting BEA-F SDCS is stated in terms of the quantities $\alpha = Q/B$, $\phi = (T/U)^{1/2}$ and $\beta = [\alpha/(4\phi) - \phi]^2$, where \bar{U} is

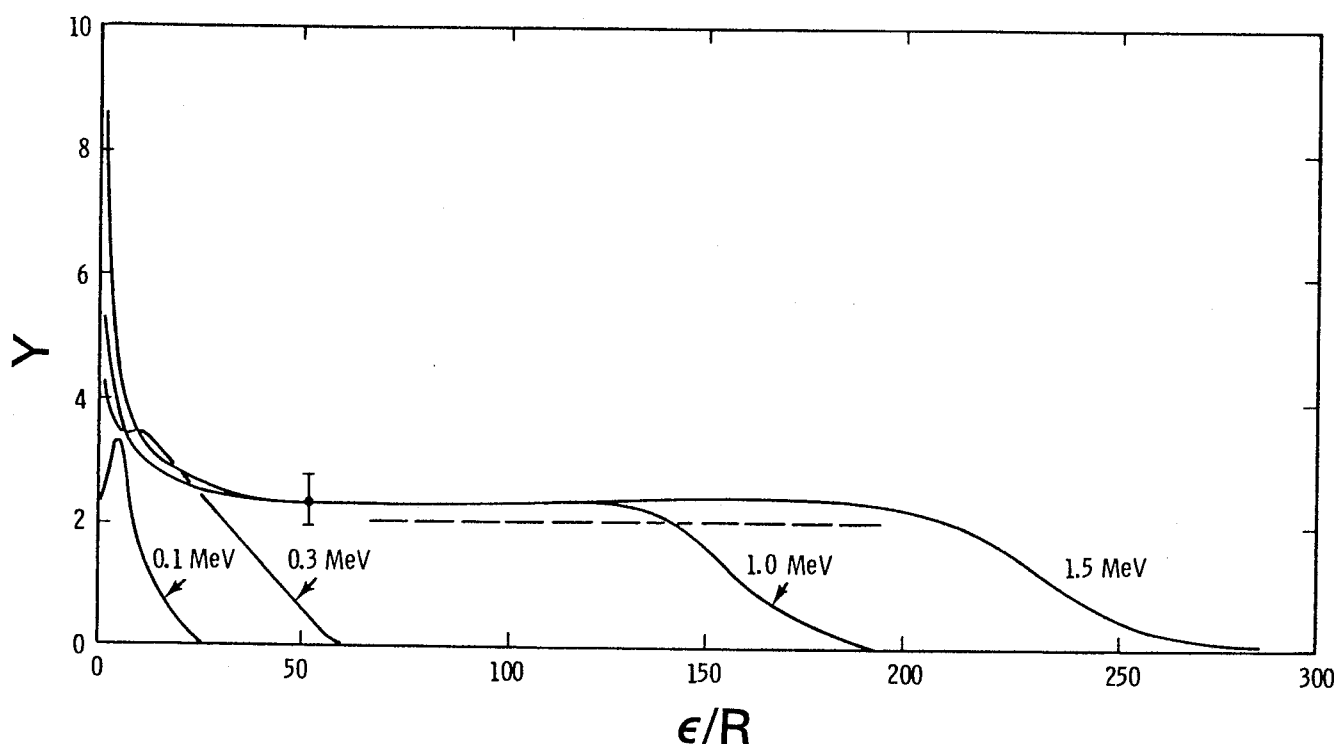


Fig. 4.8. Ratio of the measured SDCS for proton ionization of helium to the Rutherford cross section *vs.* secondary electron energy for four incident energies. Dashed line indicates expected value of 2 if the Rutherford equation were correct (from Toburen *et al.*, 1978).

the average orbital kinetic energy.

$$\begin{aligned} \sigma(Q) &= \sigma_A + \sigma_B, \text{ for } B \leq Q \leq 4T \\ &= \sigma_B, \text{ for } Q \geq 4T, \end{aligned} \quad (4.4)$$

where

$$\begin{aligned} \sigma_A &= \sigma_R(Q) \frac{\bar{U}}{\pi Q} \left[\frac{32\beta^{3/2}\alpha}{3(1+\beta)^3} \right. \\ &\quad \left. + \left(\frac{4}{3} + \alpha \right) (\pi - 2R_1) \right], \end{aligned} \quad (4.5)$$

and

$$\begin{aligned} \sigma_B &= \sigma_R(Q) \frac{\bar{U}}{\pi Q} \\ &\cdot \left[\frac{16}{3(1+\beta)^3} \left(\frac{4\phi^3}{3} - \beta^{3/2}\alpha - \frac{\alpha(\alpha+\beta)^{3/2}}{1-\alpha} \right) \right. \\ &\quad \left. + \left(\frac{4}{3} + \alpha \right) R_1 - \left(\frac{4}{3} - \frac{\alpha}{1-\alpha} \right) R_2 \right] \end{aligned} \quad (4.6)$$

and

$$R_1 = \tan^{-1} \beta^{-1/2} + \frac{\beta^{1/2}}{(1+\beta)^3} \left(1 + \frac{8}{3} \beta - \beta^2 \right) \quad (4.7)$$

and

$$\begin{aligned} R_2 &= R_3 + (1-\alpha)^{-3/2} \\ &\cdot \tan^{-1} \left(\frac{1-\alpha}{\alpha+\beta} \right)^{1/2}, \text{ for } \alpha < 1 \end{aligned} \quad (4.8)$$

$$\begin{aligned} &= R_3 + (\alpha-1)^{-3/2} \\ &\cdot \ln \frac{(\alpha+\beta)^{1/2} - (\alpha-1)^{1/2}}{(1+\beta)^{1/2}}, \text{ for } \alpha > 1 \end{aligned} \quad (4.9)$$

and

$$\begin{aligned} R_3 &= \left(2 + \frac{14}{3} \beta + \frac{8}{3} \alpha \right) \frac{(\alpha+\beta)^{1/2}}{(1+\beta)^3} \\ &\quad - \frac{(\alpha+\beta)^{1/2}}{(1+\beta)(1-\alpha)}. \end{aligned} \quad (4.10)$$

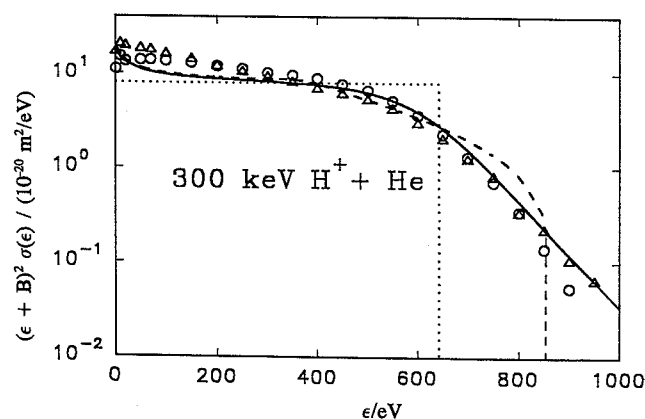


Fig. 4.9. Comparison of various calculational methods with experiment for SDCSs for electron ejection from 300-keV $H^+ + He$ collisions. SDCSs are multiplied by $(\epsilon + B)^2$ to reduce the wide range of cross sections. Circles, data of Toburen and Wilson (1975); triangles, data of Rudd *et al.* (1966b); dotted line, Rutherford equation (Eq. 2.3); dashed line, BEA (Eqs. 4.2 and 4.3); solid line, BEA-F (Eq. 4.4).

As an approximation, the average orbital kinetic energy \bar{U} may be taken to be equal to the binding energy B . Using more correct values of \bar{U} yields slightly better results. Values of \bar{U} for the subshells of several common target gases have been calculated quantum mechanically and are given in Table 2.1 along with values of N and B .

Figure 4.9 shows experimental values of SDCSs for 300 keV $H^+ + He$ compared with the predictions of the Rutherford equation, the BEA equation, and the BEA-F equation. It is clear that the Rutherford equation describes the cross sections rather poorly, especially at the low and high electron energies. The BEA yields results virtually identical to the BEA-F at low energies, but has the wrong dependence at high energies. Gryzinski (1965) rederived the classical BEA but made some additional approximations which, in some cases, improved the agreement with experiment.

Bonsen and Vriens (1970) extended the BEA to calculate angular distributions of electrons ejected by charged particles. The results, some of which are shown in Figure 4.10, agree well with experiment at intermediate angles and for ejection energies which are not too small, but have large disagreements at small and at large angles.

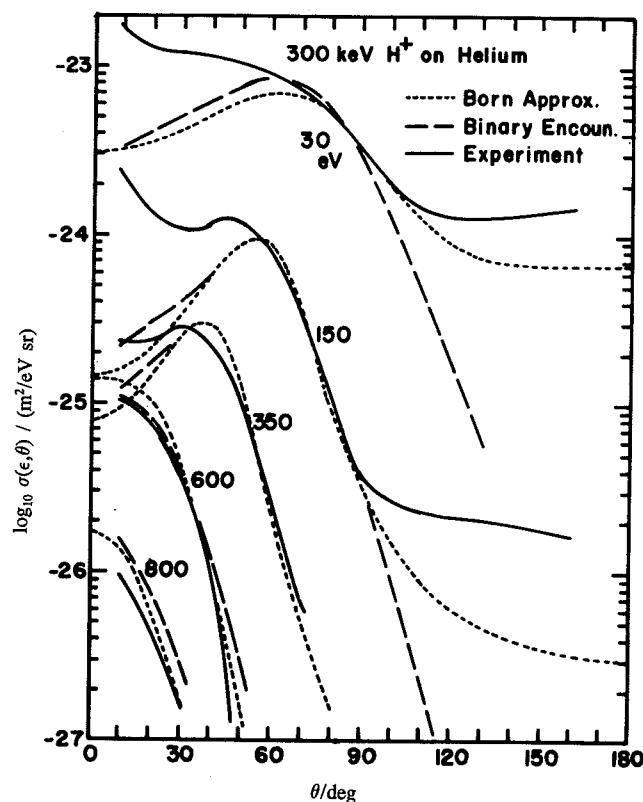


Fig. 4.10. DDCSs from 300 keV $H^+ + He$ collisions. Solid line, experiment (Rudd *et al.*, 1966b); long dashed line, BEA calculations of Bonsen and Vriens (1970); short dashed line, PWBA.

4.4.2 Quantum Mechanical Methods

Within the framework of quantum mechanics, the zero-center case is described by the Born approximation, where the outgoing electron is represented by a plane wave. But the Born approximation is more usually applied to the single-center case involving a target-centered continuum wave function and is well suited to describe the dipole-type transitions producing the soft collision peak as well as the two-body interactions creating the BE maximum.

The Born approximation was discussed in general terms in Section 2.6. The initial and final state wave functions are known analytically only for atomic hydrogen, so the calculations are often made for that target and then scaled to other targets according to the ionization potential, B . Rudd *et al.* (1966b) showed that the DDCS for a given effective charge μ , defined by

$$\mu = (B/R)^{1/2}, \quad (4.11)$$

is related to the one calculated for an atomic hydrogen target ($\mu = 1$) by the equation

$$\sigma(\epsilon, E, \mu) = (1/\mu^6) \sigma(\epsilon/\mu^2, E/\mu^2, 1). \quad (4.12)$$

In principle, then, calculations for any target can be scaled by this method to those for any other target. However, the cross sections for heavy targets are strongly underestimated in the backward directions when hydrogenic wave functions are used. This can be understood by means of the backscattering mechanism in which the ejected electron passes the target nucleus at small distances where the force exerted by the screened target nucleus is significantly larger than that given by this scaling procedure. Consequently, at backward angles, the agreement between theory and experiment can be significantly improved if more realistic potentials are used to represent the screened target center. Madison (1973) and Manson *et al.* (1975) have shown that at backward angles excellent agreement between experiment and theory can be achieved when Hartree-Slater potentials are used to derive the final continuum wave function. However, it should be emphasized that this improved agreement, obtained for proton impact, does not necessarily extend to highly charged ions.

The Born approximation underestimates the experimental data for electron ejection at forward angles, even when realistic continuum wave functions are used (Manson *et al.*, 1975; Stolterfoht *et al.*, 1987; Schneider *et al.*, 1989; Pedersen *et al.*, 1990; 1991). The enhancement of the experimental data is due to two-center effects, which can be accounted for by means of a quantum-mechanical theory based on the continuum distorted wave approximation (Crothers and McCann, 1983), discussed in Section 2.11. In this CDW-EIS theory (Fainstein and Rivarola, 1987), an

eikonal wave function and a two-center (hydrogenic) wave function are used for the initial and final states, respectively. The results are found to reproduce the experimental data at forward angles (Fainstein *et al.*, 1991b). An important future goal is the extension of two-center theory to include more realistic wave functions for the final state.

Mott and Massey (1965) gave an explicit expression for the differential cross section using the Born approximation with hydrogen wave functions. This cross section is differential in the solid angles of both projectile and ejected electron as well as the energy of the electron. Kuyatt and Jorgensen (1963) were able to do all of the needed integrations analytically to obtain the DDSCS except one which they converted to an integral over q , the momentum transfer. The result is

$$\sigma(\epsilon, \theta) = n \frac{2^8 m_p^2}{k^2} \int_{q_m}^{q_{\max}} \frac{1}{q} \frac{\mu^6 \exp \{ -2\mu/\kappa \tan^{-1} \cdot [2\kappa\mu/(q^2 - \kappa^2 + \mu^2)] \}}{[(q + \kappa)^2 + \mu^2][(q - \kappa)^2 + \mu^2][1 - \exp(-2\pi\mu/\kappa)]} \times \frac{CD^3 + 4CDE^2 - 4BD^2E - BE^3 + 2AD^3 + 3ADE^2}{(D^2 - E^2)^{7/2}} dq, \quad (4.13)$$

where

$$\begin{aligned} A &= q^2 - 2q_m \kappa \cos \theta + (\kappa^2 + \mu^2) \cdot (q_m/q)^2 \cos^2 \theta \\ B &= 2(q^2 - q_m^2)^{1/2} \kappa \sin \theta - (\kappa^2 + \mu^2)(2q_m/q^2) \cdot (q^2 - q_m^2)^{1/2} \sin \theta \cos \theta \\ C &= (\kappa^2 + \mu^2)[(q^2 - q_m^2)/q^2] \sin^2 \theta \\ D &= q^2 - 2q_m \kappa \cos \theta + \kappa^2 + \mu^2 \\ E &= 2\kappa(q^2 - q_m^2)^{1/2} \sin \theta. \end{aligned} \quad (4.14)$$

Here, θ is the angle of ejection of the electron, $q_{\min} \approx (m/2)(\kappa^2 + \mu^2)/k$, k is the wave vector for the incident proton in the laboratory system, κ is the wave vector of the ejected electron, and $q_{\max} \approx 2k$.

An example of a calculation on the Born approximation with the scaling described above is given in Figure 4.11, where it is compared with experimental values and with the BEA-F result. There is very little difference between the Born and BEA-F results in calculations of the SDSCS.

When potentials of two forces are felt by the ejected electron, the CDW-EIS model can be used. Fainstein *et al.* (1991b) have applied this model, *e.g.*, to the problem of calculating the so-called saddle-point electrons.

Senger and co-workers (Senger *et al.*, 1978; 1982) have developed a *mixed treatment* (DDCS-MT) in which they modified the Kuyatt-Jorgensen equation

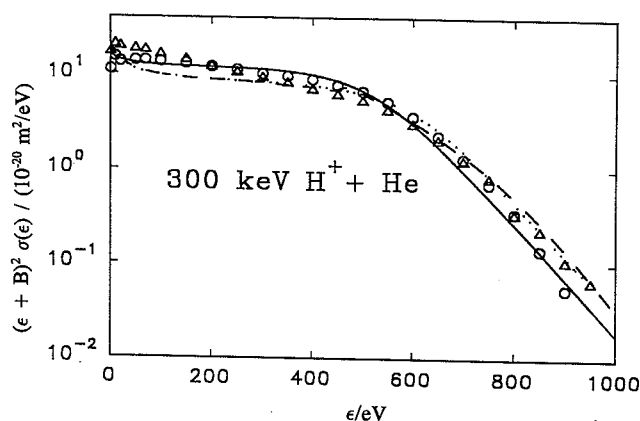


Fig. 4.11. Comparison of various calculational methods with experiment for 300-keV $H^+ + He$ collisions. Data symbols as in Fig. 4.9; dashed line, Born approximation scaled from hydrogen; dotted line, BEA-F; solid line, Rudd model (Eqs. 4.24 to 4.28).

by introducing form factors developed by Merzbacher and co-workers (Khandelwal and Merzbacher, 1966; Choi *et al.*, 1973) for inner shells. In addition, they replaced the expression for one of the parameters in that treatment by one developed empirically and also added a normalization factor. With these changes they were able to treat atoms up to $Z = 18$ with improved accuracy.

4.4.3 Semiclassical and Classical Methods

The semi-classical approximation (SCA) is a convenient method to describe electron emission in ion-atom collisions (McDowell and Coleman, 1970; Kocbach and Briggs, 1984). This approximation, which treats the motion of the collision partners classically, is expected to work well at high projectile energies (Trautmann *et al.*, 1985). The SCA in the first-order treatment is equivalent to the Born approximation for the calculation of the inelastic-collision cross section integrated over the scattering angle, and yet is justified for proton and heavier particle impact under a wider range of conditions than the Born approximation. See Section 4.4 of Inokuti (1971) and Chapter 19 of Bethe and Jackiw (1986).

The classical-trajectory Monte Carlo (CTMC) method described in Section 2.12 has been used extensively by Olson (1979) and his collaborators. Since the interactions of all three particles can be included, this method of calculation is about as good

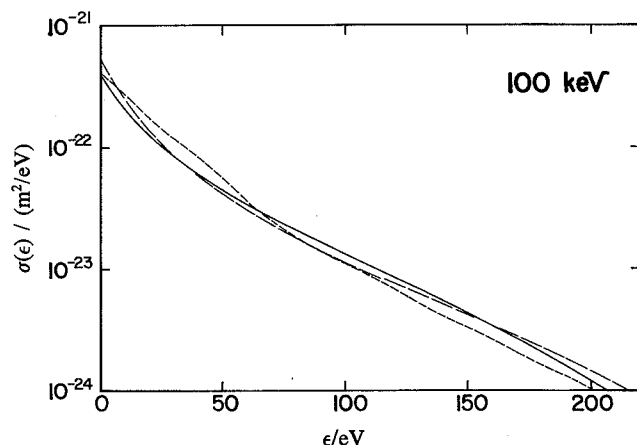


Fig. 4.12. Comparison of various calculational methods with experiment for electron emission from 100-keV $H^+ + He$ collisions. Solid line, average of experimental data; short dashed line, CTMC; long dashed line, DWBA (from Rudd *et al.*, 1992).

as is possible within the limitations of classical mechanics. The agreement with experiment, an example of which is shown in Figure 4.12, is generally quite good, especially at intermediate incident energies.

4.4.4 Screening Effects and Dielectronic Processes

Gillespie and Inokuti (1980) have discussed the role of the form factor as an index of screening. The effects of the projectile electrons have been described within the framework of the first Born approximation by Bates and Griffing (1953), Briggs and Taulbjerg (1978) and McGuire *et al.* (1981). Different contributions to the ionization cross section are distinguished in the equation

$$\sigma(\theta, \epsilon) = \sigma_M(\theta, \epsilon) + \sigma_D(\theta, \epsilon) + \sigma'_M(\theta, \epsilon) + \sigma'_D(\theta, \epsilon), \quad (4.15)$$

where M and D denote monoelectronic and dielectronic processes, respectively. The primed and unprimed quantities refer to the projectile and target, respectively. The cross sections for target ionization are given by

$$\sigma_M(\theta, \epsilon) = \frac{8\pi e^4}{\hbar^2} v_i^2 \int_{K_m}^{K_M} |Z_i - F_{0',0'}|^2 |F_{0,n}|^2 \frac{dK}{K^3}, \quad (4.16)$$

$$\sigma_D(\theta, \epsilon) = \frac{8\pi e^4}{\hbar^2 v_i^2} \int_{K_m}^{K_M} (1 - |F_{0',0'}|^2) |F_{0,n}|^2 \frac{dK}{K^3}. \quad (4.17)$$

The quantity K is the momentum transfer in the collision and $K_m = Q/v_i$ is the corresponding minimum momentum transfer already introduced in conjunction with the semiclassical model. K_M is the maximum momentum transfer. For projectile ionization the corresponding quantities $\sigma'_M(\theta, \epsilon)$ and $\sigma'_D(\theta, \epsilon)$ are obtained by interchanging the quantities associated with the projectile and target.

The expressions in 4.16 and 4.17 are evaluated by means of the form factor

$$F_{0,n}(K) = \int \phi_n(\vec{r}) e^{-iK\vec{r}} \phi_0(\vec{r}) d^3r, \quad (4.18)$$

which is associated with the single-electron transition from the initial state ϕ_0 to the final state ϕ_n . The cross sections for the dielectronic processes are obtained by integration over all final states of the projectile and target using appropriate sum rules (Bates and Griffing, 1953).

This analysis refers to a single projectile electron. If additional electrons are present, their contributions are to be included in the cross section of Eq. 4.15. In the monoelectronic process, the electron acts as part of the nucleus and, hence, adds a coherent term to that of the nucleus. In this case, $F_{0',0'}$ is replaced by the sum of form factors:

$$F_{0',0'} \rightarrow \sum_s N_s F_{0',0'}^{(s)}, \quad (4.19)$$

where $F_{0',0'}^{(s)}$ is associated with an electron in the s subshell of the incident ion and N_s is the corresponding occupation number of that subshell. On the other hand, in the dielectronic process, the electron acts independently of the projectile and thus the electron terms add incoherently. Hence, σ_D is replaced by a sum of cross sections

$$\sigma_D \rightarrow \sum_s N_s \sigma_D^{(s)}, \quad (4.20)$$

where $\sigma_D^{(s)}$ is associated with an electron in s subshell.

The form factor $F_{0',0'}$ for the projectile electron involves only bound-state wave functions. Hence, it can be readily calculated in an approximation involving scaled hydrogenic wave functions. When an electron is bound in the 1s orbital in the field of an effective charge α_p , for instance, the form factor is

$$F_{1s',1s}(K) = \frac{1}{[1 + K^2 a_0^2 / 4\alpha_p^2]^2}, \quad (4.21)$$

where a_0 is Bohr radius and α_p represents the effective projectile charge relevant for the bound electron. The form factor depends on the momentum transfer $K\hbar$ where \hbar is Planck's constant divided by 2π .

In the monoelectronic process, the predominant role of the bound electron, is the screening of the projectile nuclear charge. It is evident that without the projectile electron, the cross section from Eq. 4.15 reduces to the expression obtained from the Born approximation for a bare projectile (see Section 4.4.2). The projectile form factor describes a static negative charge cloud which reduces the incident nuclear charge. Hence, one may consider the screened projectile charge

$$q_1(K) = Z_1 - F_{0',0'}(K) \quad (4.22)$$

which enters into the integral of Eq. 4.16. However, this charge cannot be taken out of the integral since it depends on the integration variable K . Therefore, the

screening effect of the projectile electron depends on the angle and energy of the ejected electron.

The form factor, $F_{0,0}(K)$, goes to zero as $K \rightarrow \infty$, which means that for large K , the screening disappears and the cross sections for the mono-electronic process scale as Z_1^2 . This scaling is expected to apply in the binary encounter region since binary collisions generally result in a large momentum transfer.

For light incident dressed-ions (Toburen and Wilson, 1979), this scaling is correct; but for heavy dressed-ion impact (Richard *et al.*, 1990) deviations occur. For 0° BE emission, the deviations are in the form of a cross section which increases as the number of electrons bound to the projectile increases. However, for a particular projectile, theory (Schultz and Olson, 1991) predicts that the scaling in the BE region can increase, decrease, or be constant as a function of the net projectile charge. The dependence varies with the impact velocity and the emission angle. This behavior results from diffraction effects induced by the non-Coulombic field of the heavy, dressed projectile ion (Olson *et al.*, 1990; Shingal *et al.*, 1990; Reinhold *et al.*, 1990a; Bhalla and Shingal, 1991; Schultz and Olson, 1991). Such diffraction effects also lead to structure in the binary encounter peak (Kelbsch *et al.*, 1989a; 1989b). In particular situations, this structure is observed as a binary peak that splits and appears at energies unrelated to those predicted by simple kinematics.

4.5 Analytical Models

As with the electron impact data, a number of semi-empirical models have been devised which present the ion impact data in the form of an analytical equation to make the data more accessible to users. Such models are usually based on a theoretical foundation, but generally require as input a set of parameters which have been determined by fitting to experimental data. While several analytical models have been devised to fit the TICS data, few are available for the SDCSs and even fewer for the DDCSs. Four SDCS models will be discussed here, one of which also yields DDCSs. They were all devised for proton impact but usually may be extended to heavier ions with some loss of accuracy.

4.5.1 Miller Model

The Bethe equation of Eq. 2.23 is for TICSs. The corresponding equation for SDCSs

$$\sigma(Q) = 4\pi a_0^2 \frac{Z_1^2}{T} \left[\frac{R^2}{Q} \frac{df}{dQ} \ln \left(\frac{4T}{R} \right) + b(Q) \right], \quad (4.23)$$

is the basis for a model developed by Miller, *et al.*, (1983). Here df/dQ is the differential optical oscillator strength. The function $b(Q)$ is independent of the projectile energy and in this model it is determined at one projectile energy by subtraction of the soft colli-

sion term (calculated from the oscillator strength) from an experimental energy spectrum. The cross sections may then be calculated for that target at any other energy. In practice, the BEA theory is also used to help determine the form of the function $b(Q)$. Since the model is based on the Bethe theory, its use is restricted to high energy ions although it has been applied successfully to spectra from protons at energies as low as 100 keV (Miller *et al.*, 1983).

No adjustable fitting parameters are involved in this model. The input needed consists of the set of data comprising the differential optical oscillator strengths (*e.g.*, Berkowitz, 1979 and Gallagher, *et al.* 1987; 1988) and the experimental electron spectra taken at a single proton energy.

4.5.2 Rudd Model

This model for the SDCSs, given by Rudd (1988), may be used over the entire range of primary and secondary energies and is in the form of an analytic equation with parameters determined from experimental data. It is based on a simple version of the BEA equation (Eq. 4.2) which has been modified to yield the correct high energy asymptotic dependence on energy in agreement with the Bethe equation prediction. It has been further modified by the use of the promotion model for low energy collisions (Rudd, 1979). The SDCS, given in terms of the dimensionless variables $w = \epsilon/B$ and $v = (T/B)^{1/2}$, is

$$\sigma(\epsilon) = \frac{S}{B} \frac{F_1 + F_2 w}{(1+w)^3 [1 + \exp[\alpha(w - w_c)/v]]}, \quad (4.24)$$

where $w_c = 4v^2 - 2v - R/4B$, $S = 4\pi a_0^2 N(R/B)^2$ and where F_1 , F_2 , and α are adjustable fitting parameters. N is the number of electrons and B is the binding energy of electrons in a given subshell. In targets with more than one subshell, the expression is calculated individually for each subshell and then summed.

The parameter α is a constant independent of the primary energy, but it is somewhat different for different targets. The other two fitting parameters F_1 and F_2 vary systematically with proton energy and have been fitted by the following equations:

$$F_1(v) = L_1 + H_1, \quad (4.25)$$

$$\text{where } L_1 = C_1 v^{D_1} / [1 + E_1 v^{(D_1+4)}] \quad (4.26)$$

$$\text{and } H_1 = A_1 \ln(1 + v^2) / (v^2 + B_1/v^2) \quad (4.27)$$

$$\text{and } F_2(v) = L_2 H_2 / (L_2 + H_2), \quad (4.27)$$

$$\text{where } L_2 = C_2 v^{D_2} \text{ and } H_2 = A_2/v^2 + B_2/v^4. \quad (4.28)$$

The ten parameters $A_1, \dots, E_1, A_2, \dots, D_2$, and α used in Eqs. 4.24 to 4.28 yield, for a given target, the SDCS at all primary and secondary energies. These parameters have been determined for the ten targets for which sufficient data were available and are given in Table 4.1. Table 2.1 gives data on N and B . An

TABLE 4.1—Parameters for fitting SDCSs to the Rudd model, Eqs. 4.24 to 4.28^a

	He	Ne	Ar	Kr	H ₂	N ₂	O ₂	H ₂ O	CO ₂	CH ₄	Inner shells
A ₁	1.02	0.58	1.20	1.46	0.96	1.05	1.02	0.97	1.09	1.15	1.25
B ₁	2.4	65	8.0	5.7	2.6	12.0	50	82	25	14	0.50
C ₁	0.70	0.23	0.86	0.65	0.38	0.74	0.40	0.40	0.75	0.35	1.00
D ₁	1.15	0.55	0	-0.55	0.23	-0.39	0.12	-0.30	0.75	0.50	1.00
E ₁	0.70	0.16	0.80	1.00	2.2	0.80	0.30	0.38	0.65	3.0	3.0
A ₂	0.84	1.40	0.90	1.30	1.04	0.95	1.00	1.04	0.78	0.60	1.10
B ₂	6.0	0	2.7	22	5.9	1.20	5.0	17.3	3.0	3.8	1.30
C ₂	0.70	0.72	0.75	0.95	1.15	1.00	0.55	0.76	0.70	1.20	1.00
D ₂	0.50	1.35	0.80	-1.00	0.20	1.30	0	0.04	0.85	0.45	0
α	0.86	0.57	0.71	0.78	0.87	0.70	0.59	0.64	0.53	0.61	0.66

^a After Rudd *et al.* (1992).
example of the results of calculations using this model is shown in Figure 4.13, where they are compared to experimental values. While the model was devised for proton impact, it may also be used for other bare ion projectiles (provided that the interactions are not too strong) by multiplying the cross sections by Z_1^2 with the precaution that two-center and saturation effects as well as multiple ionization restrict the accuracy of this scaling procedure. This point will be discussed in Section 4.7.1.

4.5.3 Kim Model

Like the Miller model, the model proposed by Kim (see Rudd *et al.*, 1992) has as its basis the Bethe equation. Several features have been added, however, which extend the range of the model to lower proton energies and also to higher electron energies. In addition, the differential optical oscillator strengths have, for convenience, been fitted to analytical formu-

las. For these, either of two forms are used:

$$df/d(Q/R) = (R/Q) \sum_i a_i \cdot \exp \{ -[(R/Q - b_i)/c_i]^2 \} (R/Q)^{d_i} \quad (4.29)$$

or

$$df/d(Q/R) = (R/Q) \sum_i e_i (R/Q)^i, \quad (4.30)$$

where a_i, \dots, e_i are the fitting parameters. These are given in Table 4.2 for argon and nitrogen. The cross section is given as a ratio to the Rutherford cross section of Eq. 2.6, i.e., as $Y = \sigma(Q)/\sigma_R(Q)$. Thus

$$Y = \frac{Qdf/dQ \ln(4fT/R)[1 + gR/T + h(R/T)^2] + Y_{BE} + N}{1 + \exp[k(Q - 4T)/R]}, \quad (4.31)$$

TABLE 4.2—Parameters for fitting optical oscillator strength data for Ar and N₂ with Eqs. 4.29 and 4.30. The fitting was carried out on $Q(df/dQ)$, a dimensionless quantity^a

Target	Index i	a _i	b _i	c _i	d _i
Ar, M shell	1	7	0.505	0.12	0.01
Ar, M shell	2	12	0.07	0.13	1
Ar, M shell	3	0.3	0.6	0.05	1
Ar, M shell	4	11.3	0.72	0.19	3
Ar, M shell	5	10	0.63	0.1	3
N ₂ , L _A shell ^b	1	5.5	0.465	0.155	0
N ₂ , L _A shell ^b	2	0.8	0.59	0.035	0
N ₂ , L _A shell ^b	3	3.4	0.71	0.14	0
N ₂ , L _A shell ^b	4	1.3	0.81	0.09	0
N ₂ , L _A shell ^b	5	1.6	0.26	0.08	0
N ₂ , L _A shell ^b	6	10	0.11	0.1	1.1
N ₂ , L _B shell ^b	1	1.6	0.26	0.06	0
N ₂ , L _B shell ^b	2	0.7	0.36	0.055	0
N ₂ , L _B shell ^b	3	0.5	0.525	0.02	2
N ₂ , L _B shell ^b	4	0.5	0.47	0.08	1
N ₂ , L _B shell ^b	5	0.6	0.12	0.08	0.1
N ₂ , L _B shell ^b	6	0.4	0.18	0.05	1

Target	e ₁	e ₂	e ₃	e ₄
Ar, L shell	48.67	745.6	-141200	616300
N ₂ , 1σ _g + 1σ _u	2.99	5813	30506	-1987000

^a After Rudd *et al.* (1992).

^b L_A = 3σ_g + 1π_u + 2σ_u; L_B = 2σ_g.

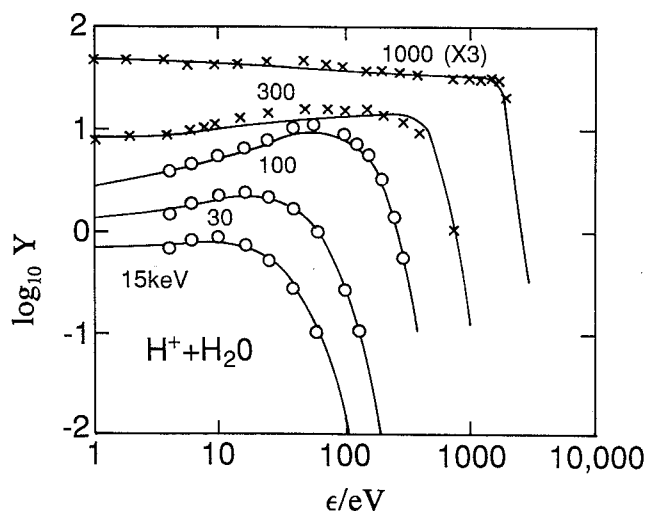


Fig. 4.13. Comparison of Rudd model calculations of electron spectra with experimental data for proton impact on water vapor at various energies. Data (crosses and circles) and calculations (lines) are plotted as Y , the ratio of the SDCS to the Rutherford cross section (from Rudd *et al.*, 1992).

where

$$Y_{BE} = \frac{NU}{Q} \left[1 - \left(\frac{U}{\epsilon + U} \right)^p \right], \quad (4.32)$$

and where f , g , h , k , and p are additional fitting parameters, N is the occupation number, and U is the average kinetic energy of the electrons in a given shell. Kim has fitted the model to argon and nitrogen (see Rudd *et al.*, 1992). The fitting parameters for those two targets are given in Table 4.3.

4.5.4 Hansen-Kocbach-Stolterfoht (HKS) Model

Hansen and Kocbach (1989) derived a simple expression for the double differential electron emission probabilities as a function of the impact parameter. The derivation was based on various model assumptions including the semi-classical approximation. The initial electron state is described by the screened hydrogenic wave function $\phi_{1s} = \pi^{-1/2} \alpha_c^{3/2} e^{-\alpha_c r}$ and a plane wave was chosen to represent the outgoing electron. This leads to the following expression which differs slightly from Eq. 6 in the paper by Hansen and Kocbach (1989):

$$P(b\theta, \epsilon) = \frac{4Z_1^2 \alpha_c^6 b^2}{\pi^2 R v_1^2 \alpha_c^3} \cdot \frac{K_1^2 [b[\alpha_c^2 + (K_m - k_t \cos \theta)^2]^{1/2}]}{\alpha_c^2 + (K_m - k_t \cos \theta)^2}, \quad (4.33)$$

where Z_1 is the charge and $v_1 = (T/R)^{1/2}$ the velocity of the projectile, $K_m = (\alpha^2 + k^2)/2v_1$ is the minimum momentum transfer, K_1 is the modified Bessel function. The quantities k_c and k_t are small modifications, which will be described later, of the quantity $k = (\epsilon/R)^{1/2}$, which is the momentum of the outgoing electron. Similarly, α_c is a modification of the mean initial momentum parameter $\alpha = (B/R)^{1/2}$, where B is the binding energy and R the Rydberg energy.

To obtain the DDCS, Eq. 4.33 is integrated over the impact parameter, $\sigma(\theta, \epsilon) = 2\pi \int P(b, \theta, \epsilon) b db$. This integration can be performed analytically, yielding a

relation of remarkable simplicity:

$$\sigma(\theta, \epsilon) = \frac{16a_0^2 Z_1^2}{3\pi R v_1^2 \alpha_c^3} \left[\frac{\alpha_c^2}{\alpha_c^2 + (\hat{K}_m - \hat{k}_t \cos \theta)^2} \right]^3, \quad (4.34)$$

where $\hat{K}_m = K_m/\alpha_c$ and $\hat{k}_t = k_t/\alpha_c$ are normalized momenta. The function in the square brackets describes the BE maximum. It resembles a Lorentzian whose width is governed by α_c . This function is the only component which involves the electron emission angle θ . Eq. 4.34 can be further integrated to obtain the SDCS:

$$\sigma(\epsilon) = \frac{8a_0^2 Z_1^2}{3R v_1^2 \alpha_c^3 \hat{k}_t} \left[\tan^{-1} \left(\frac{2\hat{k}_t}{1 + \hat{K}_m^2 - \hat{k}_t^2} \right) + \frac{5(\hat{K}_m + \hat{k}_t) + 3(\hat{K}_m - \hat{k}_t)^3}{2[1 + (\hat{K}_m + \hat{k}_t)^2]} - \frac{5(\hat{K}_m - \hat{k}_t) + 3(\hat{K}_m + \hat{k}_t)^3}{2[1 + (\hat{K}_m - \hat{k}_t)^2]} \right]. \quad (4.35)$$

These equations are for a single target electron and must be summed over all the electrons in the target. Usually only the most loosely bound outer electrons contribute appreciably, however. The original equation by Hansen and Kocbach (1989) implies that the momenta $k_c = k_t = k$ and $\alpha_c = \alpha$ but these quantities can be modified to improve the accuracy. For example, the peaking approximation, *i.e.*, the neglect of the momentum of the bound electrons in comparison to the momentum for the outgoing electron, implies that $k_c = k$ thus producing a singularity in the low-energy limit for the electron in Eqs. 4.33 through 4.35. This singularity can be removed by arbitrarily setting $k_c = (k^2 + p_0^2)^{1/2}$, where p_0 is a quantity associated with the mean momentum of the bound electron. To fit the results obtained from the Born approximation formula (Landau and Lifschitz, 1958), p_0 is chosen to yield the result

$$k_c = \left(k^2 + \frac{2\alpha^2}{\ln(2v_1/\alpha^2)} \right)^{1/2}. \quad (4.36)$$

By trial and error the parameters k_t and α_c were chosen to be

$$k_t = (k^2 + 0.2\alpha^2 \sqrt{v_1/\alpha})^{1/2}, \quad (4.37)$$

$$\alpha_c = \alpha \left(1 + 0.7 \frac{v_1^2}{v_1^2 + k^2} \right). \quad (4.38)$$

For 0.5-MeV $H^+ + He$, Figure 4.14 shows a comparison between this model and calculations with the Born approximation using screened hydrogenic wave functions (Landau and Lifschitz, 1958; Rudd *et al.*, 1966b). The BE peak at 20° is well reproduced. At other angles the agreement is not as good but still satisfactory. Figure 4.15 shows a further example for 5-MeV $H^+ + He$ collisions. In this case, the model results are compared with the Born approximation

TABLE 4.3—Parameters for fitting SDCSs to the Kim model, Eq. 4.31^a

Target	f	g	h	k	p	q	r	N
Ar, M shell	0.053	-5	20	0.1	0.3			8
Ar, L shell						0.25	0.1	8
N ₂ , L _A shell ^b	0.3	-8	25	0.1	0.2			8
N ₂ , L _B shell ^b	0.3	-8	25	0.1	0.2			2
N ₂ , 1 σ_g + 1 σ_u						1.0	0.1	4

^a After Rudd *et al.* 1992.

^b L_A and L_B are the combinations of molecular orbitals given by L_A = 3 σ_g + 1 π_u + 2 σ_u ; L_B = 2 σ_g .

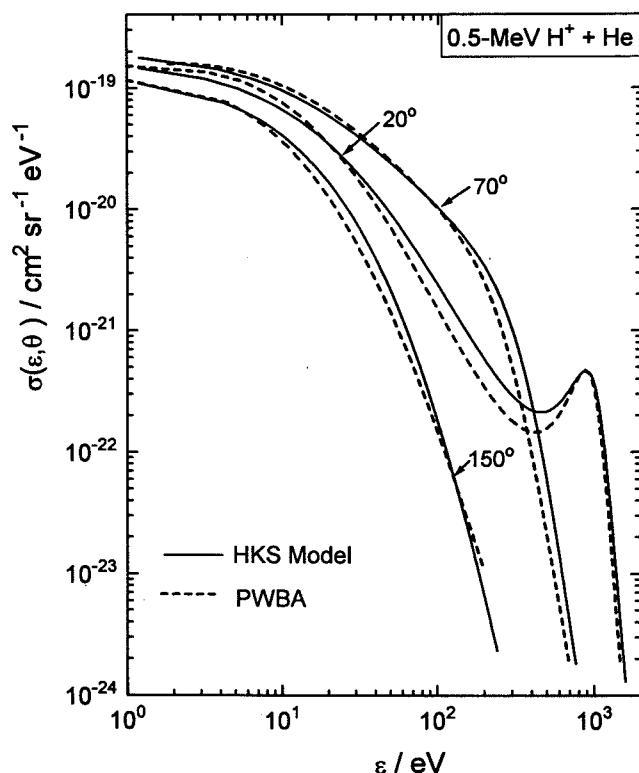


Fig. 4.14. Comparison of DDCSs for electron emission at different angles in 0.5-MeV $H^+ + He$ collisions calculated by means of the HKS-model and the plane wave Born approximation (PWBA).

using Hartree-Slater continuum wave functions for the final state (Manson *et al.*, 1975). For 30° the agreement is quite good and is still satisfactory for 90°. The SDCSs are also well reproduced as seen in Figure 4.15.

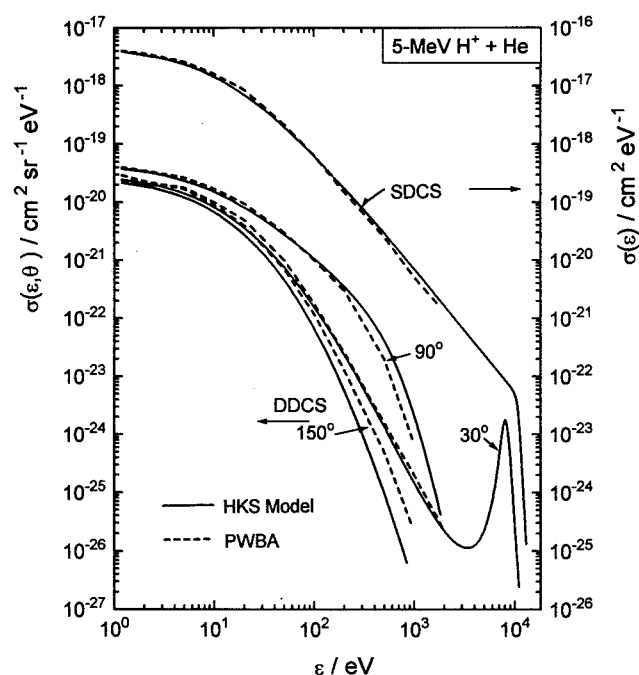


Fig. 4.15. Calculated DDCSs as in Figure 4.14 but for 5-MeV $H^+ + He$ collisions.

4.6 Proton Collisions

Even for the relatively simple case of proton ionization there is no universal method of calculation which yields accurate cross sections for all ranges of parameters for all targets. To a large extent, one must still rely on experimental data, averaged, interpolated, and correlated by the use of semi-empirical models, and tested by theoretically based consistency checks.

4.6.1 Total Ionization Cross Sections

TICSs were first measured for proton impact by Keene (1949) and most of the available experimental data were reported during the following three decades. Data of this type have been gathered and critically examined by Rudd *et al.* (1985a), who also gave recommended values for thirteen targets. Measurements and recommended values for an additional target, water vapor, were subsequently reported by Rudd *et al.* (1985b). These cross sections are conveniently given in terms of a simple fitting equation:

$$\sigma_i = (\sigma_i^{-1} + \sigma_h^{-1})^{-1}, \quad (4.39)$$

where

$$\sigma_i = 4\pi a_0^2 C x^D, \quad (4.40)$$

and

$$\sigma_h = \frac{4\pi a_0^2 [A \ln(1+x) + B]}{x}. \quad (4.41)$$

Here $x = E_p/\lambda R$, where λ is the projectile-to-electron mass ratio and R is the Rydberg energy (13.6 eV). A , B , C , and D are dimensionless adjustable fitting parameters, the values of which are given in Table 4.4 for 14 targets. These equations yield results which are quite reliable (10% or better) at high energies (greater than about 100 keV), but are less accurate at lower energies. See Rudd *et al.* (1985a) for further details.

TABLE 4.4—Values of parameters for fitting TICSs to Eq. 4.39

Target	A	B	C	D
H	0.28	1.15	0.44	0.907
He	0.49	0.62	0.13	1.52
Ne	1.63	0.73	0.31	1.14
Ar	3.85	1.98	1.89	0.89
Kr	5.67	5.50	2.42	0.65
Xe	7.33	11.1	4.12	0.41
H ₂	0.71	1.63	0.51	1.24
N ₂	3.82	2.78	1.80	0.70
O ₂	4.77	0.00	1.76	0.93
CO	3.67	2.79	2.08	1.05
CO ₂	6.55	0.00	3.74	1.16
NH ₃	4.01	0.00	1.73	1.02
CH ₄	4.55	2.07	2.54	1.08
H ₂ O	2.98	4.42	1.48	0.75

4.6.2 Recommended Singly Differential Cross Sections

Rudd *et al.* (1992) have reviewed reports giving the energy spectra of secondary electrons from proton collisions. A summary of the papers on differential cross sections is given in Table 4.5, which includes only those reports which cover a wide range of angles. Measurements made by the energy loss method are included, but conference proceedings which repeat data reported elsewhere have been omitted. A considerable amount of DDCS data has accumulated which covers a fairly wide range of angles and secondary electron energies, but data over a complete primary energy range of a few keV to a few MeV are available only for helium, argon, and water vapor, although data on hydrogen and nitrogen have been published up to about 1500 keV. The data are extensive enough for ten of the target gases that the Rudd model for the SDCS has been fitted to the data and the parameters determined. These are given in Table 4.1.

Reviews of proton differential cross sections have been made by Rudd and Macek (1972), Ogurtsov (1972), Stolterfoht (1978), and by Toburen and Wilson (1979) and Toburen (1982; 1990). Rudd *et al.* (1976; 1979) have published compilations of experimental differential cross section data for helium and argon.

While the use of the Rutherford cross section, as given in Eq. 2.3, is attractive because of its simplicity, there are severe limitations on its accuracy as demonstrated in Figures 4.8 and 4.9. It should not be used at all at low primary velocities, say below 100 keV/u, and it has the wrong projectile energy dependence at high energies. Because it is usually used with a sharp kinematic cutoff of secondary energies, it yields no cross sections above that point. The BEA result embodied in Eqs. 4.2 and 4.3 and the BEA-F result of Eq. 4.4 yield much better results.

Many different quantum mechanical methods have been applied to the collision problem. The PWBA is relatively accessible using Eq. 4.13 and 4.14. The distorted-wave Born approximation (DWBA) is discussed in the review by Rudd *et al.* (1985a).

The CTMC method described in Sections 2.12 and 4.4.3 can be expected to give SDCSs for helium with an accuracy of about 10% in the intermediate energy range (~400 keV) but will yield less reliable cross sections at both higher and lower energies. Unfortunately, the application of this method is not straightforward, but involves the statistical interpretation of the results of thousands of individual orbit calculations.

The Rudd model, given by Eqs. 4.24 to 4.28, is easily accessible to users when the parameters have been determined for the particular target of interest. This, in fact, is the only model that yields reasonably accurate SDCSs at proton energies below 100 keV.

TABLE 4.5—Differential proton ionization data available^a

Energy keV	Reference
Atomic Hydrogen (H)	
25–200	Park <i>et al.</i> (1977)
20–200	Park (1983)
Helium (He)	
50–150	Rudd and Jorgensen (1963)
100–300	Rudd <i>et al.</i> (1966b)
25–125	Park and Schowengerdt (1969b)
300–500	Stolterfoht (1971a)
300–5000	Manson <i>et al.</i> (1975)
5–100	Rudd and Madison (1976)
300–1500	Toburen <i>et al.</i> (1978)
5–30	Tokoro and Oda (1985)
20–100	Gibson and Reid (1986)
7.5–150	Cheng <i>et al.</i> (1989a)
50–100	Bernardi <i>et al.</i> (1989)
100–200	Bernardi <i>et al.</i> (1994)
Neon	
50–300	Crooks and Rudd (1971)
300–1500	Toburen <i>et al.</i> (1978)
7.5–150	Cheng <i>et al.</i> (1989a)
106	Suárez <i>et al.</i> (1993b)
106	Suárez <i>et al.</i> (1993c)
Argon	
50–300	Crooks and Rudd (1971)
300–500	Gabler <i>et al.</i> (1974)
5–50	Criswell <i>et al.</i> (1977)
5–70	Rudd (1977)
250–4200	Toburen <i>et al.</i> (1978)
50	Gibson and Reid (1987)
Krypton	
7.5–150	Cheng <i>et al.</i> (1989a)
Xenon	
300–2000	Toburen (1974)
Molecular Hydrogen (H ₂)	
50–100	Kuyatt and Jorgensen (1963)
100	Rudd and Jorgensen (1963)
100–300	Rudd <i>et al.</i> (1966b)
300–1500	Toburen and Wilson (1972)
5–100	Rudd (1979)
50	Gibson and Reid (1987)
Nitrogen (N ₂)	
50–300	Crooks and Rudd (1971)
200–500	Stolterfoht (1971b)
300–1700	Toburen (1971)
300	Toburen and Wilson (1975)
5–70	Rudd (1979)
50	Gibson and Reid (1987)
Oxygen (O ₂)	
50–300	Crooks and Rudd (1971)
7.5–150	Cheng <i>et al.</i> (1989b)
50	Gibson and Reid (1987)
Water (H ₂ O)	
300–1500	Toburen and Wilson (1977b)
3000, 4200	Wilson <i>et al.</i> (1984)
15–150	Bolorizadeh and Rudd (1986b)
50	Gibson and Reid (1987)
Carbon Dioxide (CO ₂)	
50	Gibson and Reid (1987)
7.5–150	Cheng <i>et al.</i> (1989b)
Ammonia (NH ₃)	
250–2000	Lynch <i>et al.</i> (1976)
3000–4200	Wilson <i>et al.</i> (1984)
Sulfur Hexafluoride (SF ₆)	
300–1800	Toburen <i>et al.</i> (1977c)
Tellurium Hexafluoride (TeF ₆)	
300–1800	Toburen <i>et al.</i> (1977c)

TABLE 4.5—Continued

Energy keV	Reference
Methane (CH ₄)	
200–400	Stolterfoht (1971a)
250–2000	Lynch <i>et al.</i> (1976)
3000, 4200	Wilson <i>et al.</i> (1984)
50	Gibson and Reid (1987)
Acetylene (C ₂ H ₂)	
300–1000	Wilson and Toburen (1975)
Ethylene (C ₂ H ₄)	
300–1000	Wilson and Toburen (1975)
Ethane (C ₂ H ₆)	
300–1000	Wilson and Toburen (1975)
Benzene (C ₆ H ₆)	
300–2000	Wilson and Toburen (1975)
Monomethylamine (CH ₃ NH ₂)	
250–2000	Lynch <i>et al.</i> (1976)
Dimethylamine [(CH ₃) ₂ NH]	
250–2000	Lynch <i>et al.</i> (1976)

^a After Rudd *et al.* (1992).

For greater accuracy at higher energies the Kim model, Eq. 4.31, should be used. Unfortunately, the parameters for that model have been determined only for argon and nitrogen. These are given in Tables 4.2 and 4.3. The HKS model is convenient to use, has no adjustable parameters, and gives both DDCSs and SDCSs. However, it is a new model which has been tested only for a few cases.

4.6.3 Recommended Doubly Differential Cross Sections

Progress in developing accurate descriptions of the angular distributions of secondary electrons has been much slower than that for the energy distributions. The DDCSs, which embody the angular distributions, have been calculated by binary encounter methods but the results are extremely poor in the backward hemisphere and somewhat inaccurate at small angles as seen in Figure 4.11. Quantum mechanical methods are better, provided one uses accurate wave functions. Eq. 4.34 of the HKS semi-empirical model yields DDCSs and this method, while untested, appears to be very promising. As is the case with most treatments, this model does not account for electron capture to the continuum, so the cross sections near the ECC peak are not accurate.

4.7 Heavy Ion and Neutral Collisions

4.7.1 Target Ionization by Bare Projectiles

The mechanisms of ionization by bare heavy projectiles are similar to those discussed previously for proton impact. The electron spectra induced by heavy ions generally also exhibit the maxima due to soft and binary collisions (Figure 4.2). At electron observation

angles near 0°, heavy ions as well as protons produce the cusp peak due to ECC.

The Born approximation and other theoretical treatments suggest that the cross sections scale as Z_1^2 , but as Z_1 increases, this scaling ultimately fails, partly because the ionization probabilities approach unity so the cross sections saturate at values smaller than those predicted by Z_1^2 scaling. Large ionization probabilities also mean that multiple target ionization becomes important and multiple ionization does not scale as Z_1^2 . Bare, heavy ion-induced cross sections also deviate from scaled proton cross sections because two-center effects become more important. Unlike proton impact, highly charged ions create two-center effects in the ejected electron spectra at nearly all emission angles.

A necessary criterion for applying first order perturbation theories, which predict Z_1^2 scaling, is that the ionization probabilities must be small. Theory predicts that differential and total single target ionization cross sections scale essentially as $(Z_1 v_0/v_1)^2$ where Z_1 is the projectile nuclear charge and v_1 and v_0 are the impact and Bohr orbital speeds, respectively. A condition for applying this approximation is that $Z_1 v_0/v_1 \ll 1$, which means that for a given impact speed, Z_1^2 scaling is expected only for Z_1 less than some maximum value. This is demonstrated in Figure 4.16, where ratios of calculated TICSs of helium are shown. The cross sections for bare ion impact are divided by proton impact cross sections and by Z_1^2 . For large v_1 , these scaled cross sections approach a limiting value of 1, meaning that Z_1^2 scaling applies. But for smaller values of v_1 the ratios are smaller than 1 indicating that the bare heavy ion cross sections are smaller than scaled proton cross sections. The deviation increases with decreasing impact speed and with increasing projectile charge, Z_1 , because these conditions imply increasing ionization probabilities. In

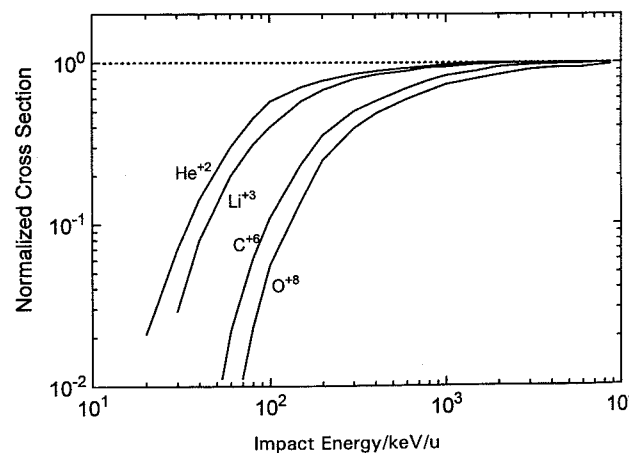


Fig. 4.16. TICSs for heavy bare ion impact divided by proton impact cross sections and by Z_1^2 , where Z_1 is the heavy ion nuclear charge. The cross sections are calculated using the CDW-EI theory (Fainstein *et al.*, 1991a).

these circumstances, the differential cross sections for electron emission will also be affected.

Since the PWBA represents only one-center effects, TCEE results in deviations between experiment and the PWBA. In Figure 4.17, such a comparison is shown for electron emission in 25-MeV Mo^{40+} impact on He measured at different observation angles. For angles around 90° theory and experiment agree in the energy range above 100 eV. This is because at those angles and energies the dominant part of the electron emission is produced by binary collisions whose description is incorporated in the PWBA. The BE maximum is visible for electron emission at forward angles but BE electrons may also appear at angles somewhat larger than 90° when the electron is deflected by the field of the target nucleus. This effect is also incorporated in the PWBA which accounts for all interactions with the target nucleus.

At angles much different from 90° , however, the experimental cross sections deviate from the scaled H^+ data by factors as large as 5. Relative to the PWBA the experimental cross sections are enhanced at forward angles and reduced at backward angles as seen in Figure 4.18. These discrepancies can be attributed to two-center effects in which the field of the projectile nucleus plays an important role as the electrons emerge from the target center. Two-center effects are described qualitatively by the CDW-EIS calculations (Fainstein and Rivarola, 1987) as shown in Figure 4.18.

Two-center effects are more important for high secondary energies because a fast electron feels the two-center field of the rapidly disintegrating collision system more strongly than an electron which emerges so slowly from the target that the projectile is already

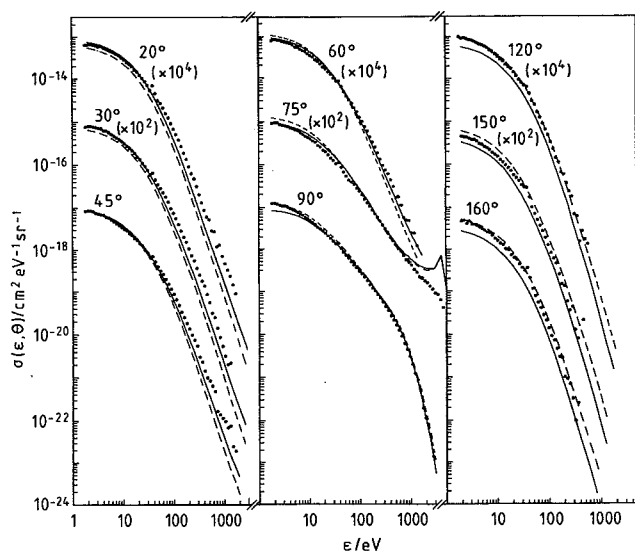


Fig. 4.17. Cross sections for electron emission in collisions of 25-MeV/u Mo^{40+} on He for different observation angles. Data points, experimental values; solid lines, CDW theory; dashed lines, PWBA (after Stolterfoht *et al.*, 1987).

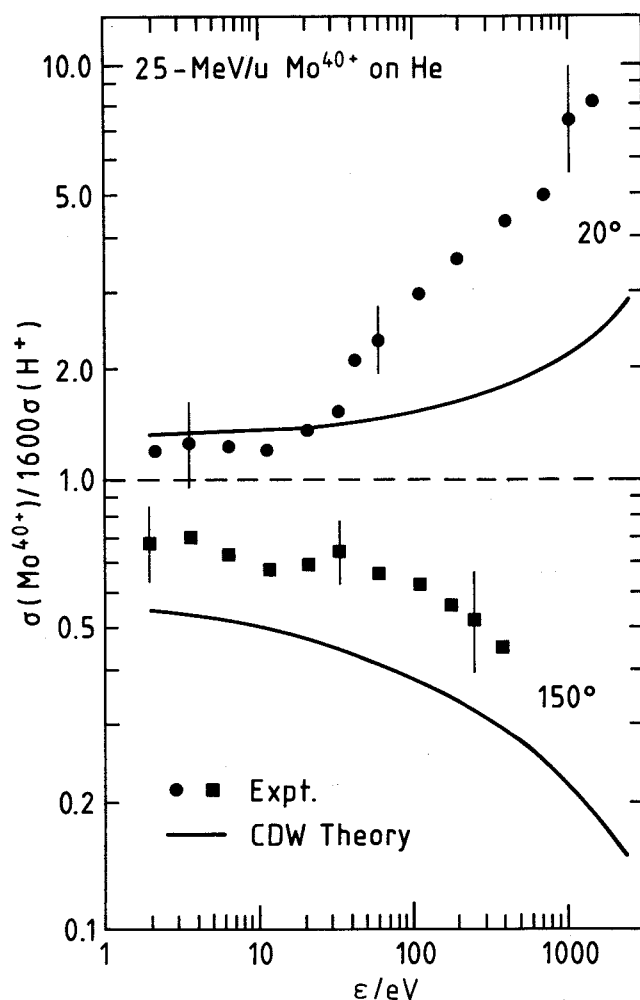


Fig. 4.18. DDCSs for electron emission by 25-MeV/u Mo^{40+} divided by Z_1^2 and by the DDCS for H^+ impact on He. Observation angles are 20° and 150° . Points, experimental results for Mo^{40+} , and H^+ cross sections calculated by the PWBA; solid line, calculations using the CDW-EIS theory (Fainstein and Rivarola, 1987). Between 30 to 40 eV the data are influenced by autoionization electrons (from Stolterfoht *et al.*, 1987).

far away. Two-center effects are significant for electrons which are ejected with at least half the speed of the projectile (Meckbach *et al.*, 1986). An electron leaving the target center is deflected by the field of the projectile nucleus (Figure 4.1), which enhances the electron intensity at forward angles and reduces it at backward angles. The surprisingly large reduction is due to the high charge state of the projectile. The ejected electron is evidently affected even when it moves rapidly in a direction opposite to that of the projectile.

The total ionization cross section for a bare ion with a relativistic speed is given by Eq. 2.29, which uses the projectile speed v (through $\beta=v/c$) rather than its kinetic energy E . Similarly, the relativistic form of the Rutherford cross section, Eq. 2.3, is given by Eq. 2.31 by keeping only the first term in the square brackets on the right-hand side. Eq. 2.31 is also

correct when the ejected electron energy is relativistic.

4.7.2 Target Ionization by Dressed Projectiles

When a projectile carries electrons, the electron spectra contain additional features. Figure 4.19 shows examples for results obtained in 30-MeV $O^{5+} + O_2$ collisions for a variety of observation angles (Stolterfoht *et al.*, 1974). (Note that the cross sections have been multiplied by the electron energy.) The soft-collision and binary-encounter peaks result from ionization of the target and the peak labeled "O-K Auger (T)" is due to Auger electron emission from the target. The K-Auger electrons ejected from the projectile are influenced by the kinematic effect so that their position varies with observation angle. Under some

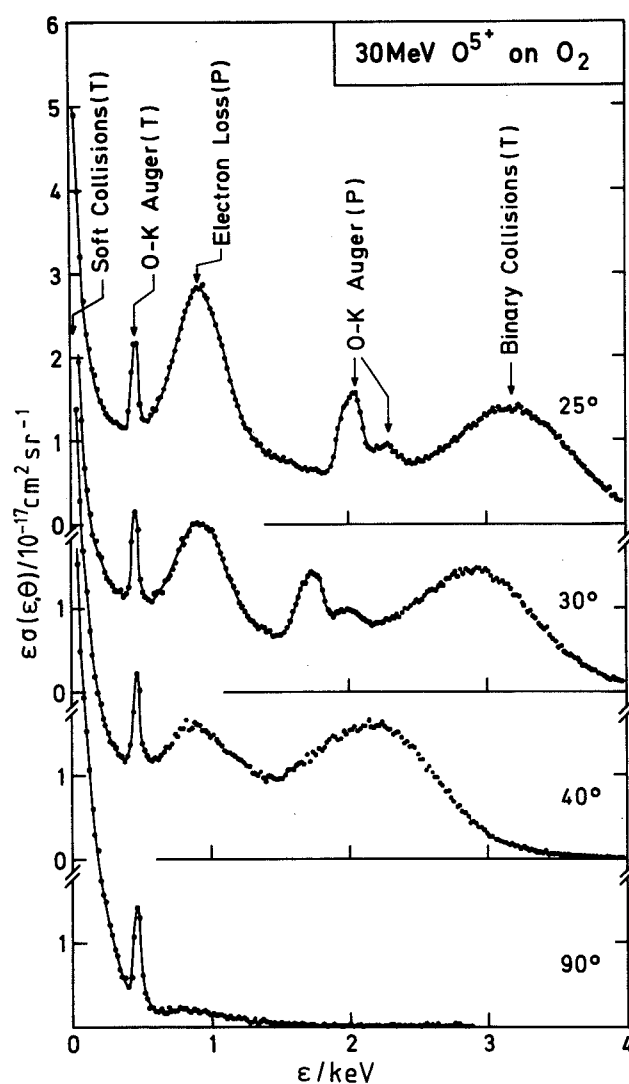


Fig. 4.19. Doubly differential cross section for electron emission in collisions of 30-MeV O^{5+} with O_2 multiplied by the electron energy. The electrons are observed at different angles as indicated. (T) and (P) indicate peaks due to electrons from the target and projectile, respectively (from Stolterfoht *et al.*, 1974).

conditions kinematic effects can produce two projectile Auger peaks for a single transition.

Figure 4.20 shows an additional example of the screening effects produced by a 1s electron for 0.5-MeV/u He^+ incident on He (Manson and Toburen, 1981). The screened charge is $q_1 = 2 - F_{1s',1s'}$ where $F_{1s',1s'}$ follows from Eq. 4.14 with $\alpha_p = 2$. At low electron energies the screened data follow the results for H^+ impact whereas at high electron energies they approach the results for He^{2+} impact since, as seen from Eq. 4.21, the screening tends to the maximum value of 1 for small K but vanishes for large K .

To estimate screening effects an approximate expression is needed which factorizes the contributions for the target and projectile outside the integral of Eq. 4.16. This could be achieved by replacing the screened nuclear charge $q_1(K)$ by a constant value \bar{q}_1 determined for the average momentum transfer. Eq. 4.16 indicates that the average momentum transfer is governed by the expression $F_{0,n}(K)/K^3$ which increases strongly with decreasing K . Hence, we determine the constant form factor \bar{q}_1 by means of a value $K \approx K_m$ close to the minimum momentum transfer. However, since this assumes that the screening effects are independent of the electron emission angle and since screening effects may influence the angular distribution of the electrons (Manson and Toburen,

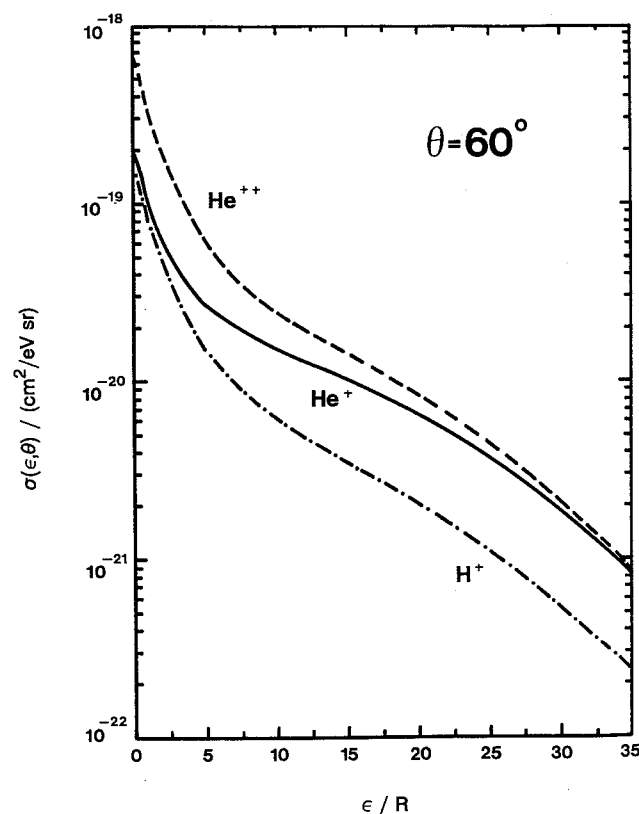


Fig. 4.20. Calculated DDCSs for electron production at 60° by 0.5-MeV/u H^+ , He^+ , and He^{2+} colliding with He. The He^+ data exhibits the variation of screening effects of the projectile electron with secondary energy (from Manson and Toburen, 1981).

1981), this method is only an approximation. An analysis of screening effects by means of the adiabatic radius R_{ad} has been performed for the collision system 30-MeV $O^{q+} + O_2$ (Stolterfoht *et al.*, 1974). The results are shown in Figure 4.21, where the cross sections obtained with dressed projectiles O^{q+} are normalized to those of the bare projectile O^{8+} . At low electron energies, the screened cross sections are determined by the projectile charge q , whereas at high energies they are governed by the charge $q = 8$ of the bare projectile.

In the previous analysis of screening effects, dielectronic processes were disregarded. Screening tends to decrease the cross sections for electron emission since it reduces the strength of the perturbing projectile. However, the cross sections may be enhanced by dielectronic processes as the incident electron provides an incoherent contribution to the target ionization. This enhancement of the cross sections can be seen in the angular distributions of Figure 4.22. Cross sections σ_M and σ_D for target ionization were calculated assuming that the projectile electron remains in the ground state (curve C) or is excited or ionized (curve D), respectively. See Eqs. 4.16 and 4.17. The dielectronic processes represented by curve D provide a significant contribution to the cross section.

There have been only a few studies of the role of dielectronic processes in electron emission by heavy particles. Recent progress in understanding the interaction between projectile and target electrons in

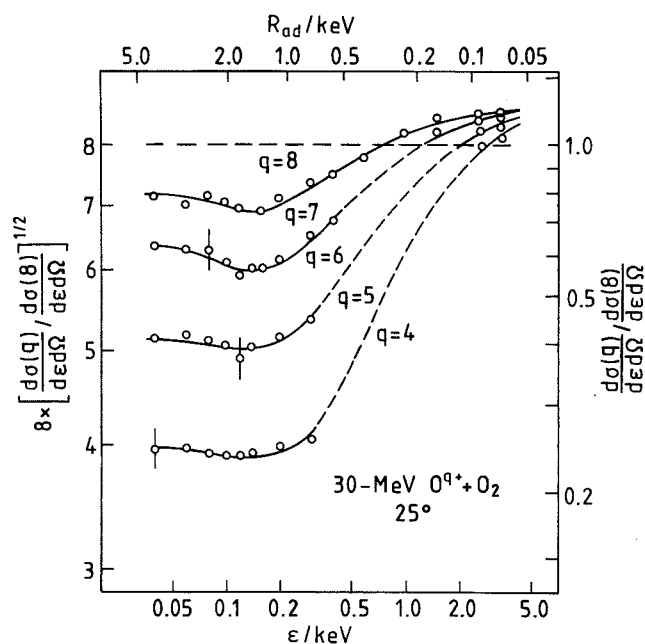


Fig. 4.21. Relative cross section for electron emission at 25° in 30-MeV $O^{q+} + O_2$ collisions. The data for $q=4$ to 7 are normalized to those of the bare projectile ($q=8$). The data exhibits the screening effects of the projectile electrons as a function of the ejected electron energy (from Stolterfoht, 1978).

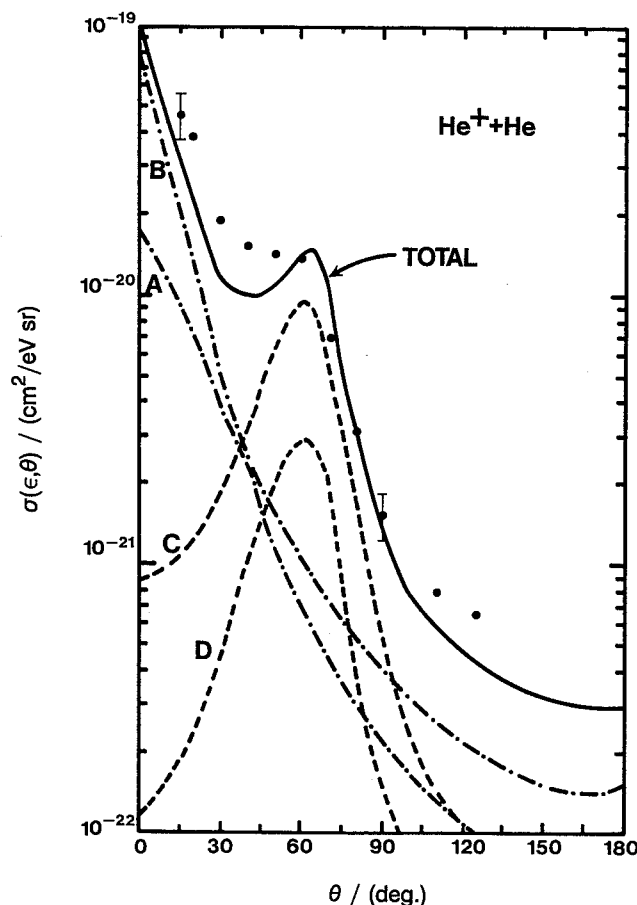


Fig. 4.22. Calculated DDCSs for emission of 218-eV electrons from the projectile and target in 0.5-MeV/u $He^{+} + He$ collisions. A, projectile ionization with the target remaining in the ground state; B, projectile ionization with simultaneous target excitation; C, target ionization with the projectile remaining in the ground state; D, target ionization with simultaneous projectile ionization (from Manson and Toburen, 1981).

energetic ion-atom collisions originates from investigations of TICSs (see, *e.g.*, Meyerhof and Hülskötter, 1991). Dielectronic processes may cause the release of electrons from the projectile which contribute to the measured electron spectra as discussed in the next subsection.

4.7.3 Electron Emission from the Projectile

In addition to the dielectronic process, projectile electron emission may be caused by the interaction with the target nucleus. There is no essential difference between target and projectile, so when projectile ionization, *i.e.*, electron loss, is treated, the collision system can be regarded as being reversed. Thus, the formalism presented above is valid for electron loss as well as for target ionization. Two differences, however, must be taken into account. First, the screening effects for the neutral target are significant. The long-range dipole interaction characteristic of incident ions is not important for projectile ionization. Second, the electrons ejected from the moving projec-

tile are influenced by kinematic effects. In fact, electrons ejected from the moving projectile are changed in energy, angle, and intensity as described in detail by Rudd and Macek (1972) and by Stolterfoht (1987).

In Figure 4.19 the most pronounced maxima are due to the electron-loss mechanisms in which electrons from the projectile are ejected with a laboratory speed equal to that of the projectile (Burch *et al.*, 1973). To first order, it follows that the centroid energy of the electron loss peak is $\epsilon_{BE} = T$. Hence, its energy is independent of the observation angle. However, its intensity decreases strongly as the observation angle increases. The angular dependence is understood by a simple picture in which quasi-free projectile electrons are elastically scattered in the Coulomb field of the target (Wilson and Toburen, 1973). Indeed, according to the treatment by Rutherford (1911), elastically scattered electrons are strongly concentrated in the forward direction. This scattering mechanism is the same as that for the BE electron emission (Figure 4.1). Both mechanisms may be understood on the basis of the impulse approximation with the roles of target and projectile interchanged.

Further examples of cross sections for projectile electron emission are given in Figure 4.22 for the collision system 0.5-MeV/u $\text{He}^+ + \text{He}$. The electron energy of 218 eV was chosen to achieve a near velocity matching of the ejected electron with the projectile (Manson and Toburen, 1981). In this case, the electron energy ϵ' in the projectile frame is rather small and the laboratory cross section reaches a maximum at small observation angles. Indeed, the curves A and B, referring to the projectile ionization cross sections σ'_M and σ'_D in Eq. 4.15, respectively, exhibit a strong increase near the limit of zero angle in the laboratory frame. Curve A represents the case where the target electron remains in its ground state during the collision, whereas curve B is for the case where the target electron is excited or ionized. The latter case corresponds to a two-electron process induced by the electron-electron interaction, *i.e.*, the dielectronic process.

At small angles, the dielectronic process is much stronger than the mono-electronic process due to the dominance of distant collisions which create low-energy electrons in the projectile frame resulting in electrons ejected in the forward direction in the laboratory frame. In this case, the screening effects for the neutral target are considerable so that the mono-electronic process is strongly reduced and the dielectronic process becomes dominant. In certain regions of the energy and angular distributions, significantly greater numbers of electrons are produced by dielectronic processes than by interaction with the screened target nucleus.

4.7.4 Effective Charge of Energetic Ions

In the process of slowing, energetic charged particles undergo a series of electron capture and loss events contributing to a changing equilibrium charge that may be quite different from their bare nuclear charge; in the extreme case, at low energies, the moving particle may become neutral. Electrons bound to the projectile screen its nuclear charge reducing the potential for interaction with media electrons, thus reducing the stopping power of the projectile. In stopping power theory, the *effective charge* of the moving ion was a concept introduced to scale stopping power values for bare ions to ions that have become partially screened by bound electrons. The effective charge is primarily a function of the projectile velocity and nuclear charge. Numerous models have been developed to determine an effective charge appropriate to ions possessing bound electrons (Bohr, 1940; 1941; Kreussler *et al.* 1981; Anthony and Lanford, 1982; Barkas, 1963; Bichsel, 1990a). The measured electron spectra produced by ionizing collisions provide an opportunity to test these models because electron ejection represents a major contribution to stopping power, see, *e.g.*, Section 6.5. By using the results of Eq. 6.3, assuming excitation makes a negligible contribution to the stopping power, comparing particles of equal speed, and recalling that stopping power is proportional to Z_{eff}^2 , one can define the effective charge of any partially dressed ion A^{n+} relative to that for protons ($Z_1 = 1$) as

$$Z_{\text{eff}} = \left[\frac{[(B + \bar{\epsilon})\sigma_i]_{A^{n+}}}{[(B + \bar{\epsilon})\sigma_i]_{H^+}} \right]^{1/2} \quad (4.42)$$

Equation 4.42 can be evaluated for any collision system where the differential cross sections or the mean energy for electron emission are known for both the ion in question and for the equivalent velocity proton. When this expression is used to determine the effective charge of a 1.2-MeV C^+ ion from the data of Toburen *et al.* (1990b), illustrated in Figure 4.23, the Z_{eff} derived is approximately 2.7 and increases with increasing ion energy. This example illustrates that the effective charge of a moving ion, with respect to energy loss, is somewhat larger than the actual charge on a moving ion. This difference results because screening of the nuclear charge of the projectile by its bound electrons is not 100% efficient. Similar results were presented in the work of Brandt and Kitagawa (1982), where the stopping powers for different ions were compared.

This interpretation of the interaction of dressed ions with the medium through which they pass differs from the more traditional viewpoint that the effective charge of the moving particle is equal to the instantaneous charge on the moving ion. If one were to take the traditional assumption literally, however, a slow ion that has become neutralized by electron capture would not be expected to interact in any way with the

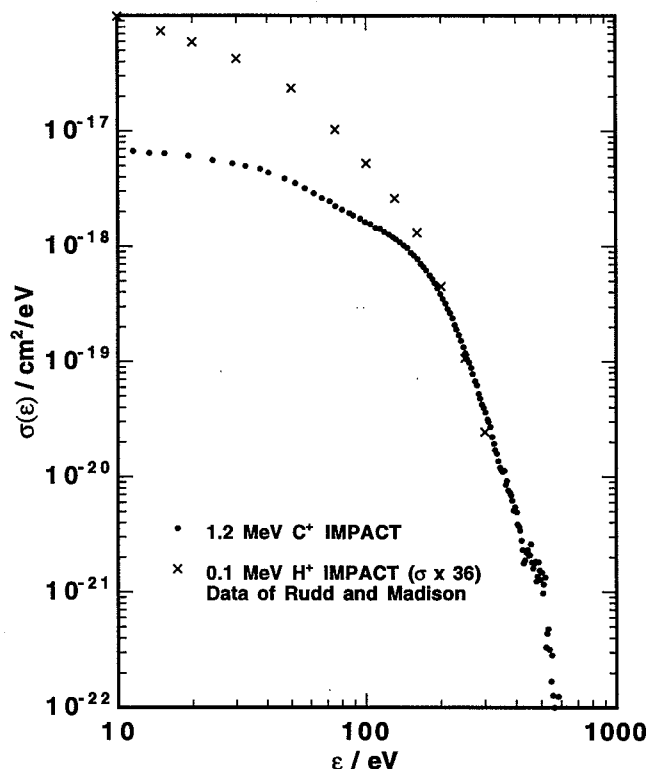


Fig. 4.23. SDCSs for ionization of helium by protons and singly charged carbon ions. The proton data are multiplied by 36 to scale according to Z_1^2 as suggested by Rutherford theory. Proton data, Rudd and Madison (1976); carbon ion data, Toburen *et al.* (1990b).

electrons of the medium through which it is traveling. This assumption is shown to be erroneous in Figure 4.24, where the spectrum of electrons ejected by neutral hydrogen and helium projectiles is compared to similar data for equal velocity protons; for comparison to the He ion data the proton cross sections have been scaled by a factor of 4. The cross sections for ejection of fast electrons (*i.e.*, for $\epsilon \geq 400$ eV) by H^0 impact (or for He^0 impact), are in excellent agreement with the proton (or scaled proton) cross sections. This occurs because these energetic electrons are ejected in small impact parameter collisions where the screening of the projectile nucleus by its bound electron(s) is inefficient. For the lowest energy ejected electrons, resulting from large impact parameter collisions, one may expect the projectile screening to be most efficient. However, even at the lowest electron energies shown here (and at energies as low as a few eV in measurements with neutral hydrogen projectiles by Bolorizadeh and Rudd, 1986c), the ionization efficiency of the neutral hydrogen projectile is nearly equivalent to that of the bare proton. For the neutral helium projectile, the ionization efficiency is reduced to about that of an unscaled proton at an electron energy of about 50 eV.

In measurements that observe electrons of even lower energies (Bolorizadeh and Rudd, 1986c), the cross sections for ionization by neutral projectiles

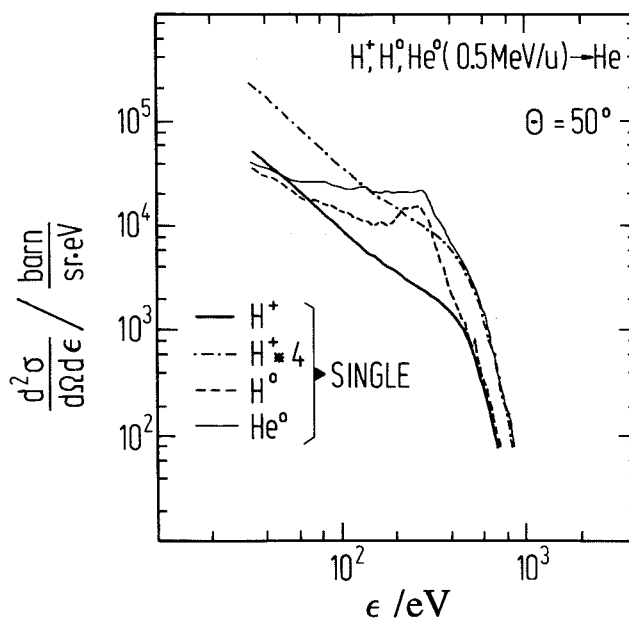


Fig. 4.24. DDCSs for the ionization of He by H^0 , H^+ , He^0 , and H^+ times 4. The peaks in the spectra at about 225 eV for H^0 and He^0 impact are due to electron loss from the projectile (after Heil *et al.*, 1992).

may actually be larger than those for protons. This enhancement is attributed to contributions from direct interactions of the bound projectile electrons with the target electrons.

The peak observed in Figure 4.24 in the ejected electron distributions for electrons ejected at about 275 eV is due to electrons stripped from the projectile. Those electrons have a speed in the laboratory frame equal to the speed of the ion from which they were stripped and will be predominantly emitted at small emission angles.

The conclusions to be drawn from the data in Figure 4.24 are that one must be cautious when assuming that the effective charge appropriate for stopping power calculations is equal to the mean ionic charge. Although the example shown in Figure 4.24 is a special case of interactions involving a pure charge state while actual stopping power measurements record the energy loss for an equilibrium charge distribution, one must still be aware of the difference between the effective charge and an equilibrium charge if accurate stopping power values are to be extrapolated from known equilibrium charge states and known bare-ion stopping powers.

The difference between the mean equilibrium charge state \bar{q} of an ion passing through a gas and the effective charge Z_{eff} determined from stopping power data is illustrated in Figure 4.25 as a function of ion velocity for the case of proton impact. In this example, average effective charges from stopping power are derived from the analysis of Yarlagadda *et al.* (1978) and the model of Barkas (1963). The mean equilibrium ion charge is taken from charge transfer mea-

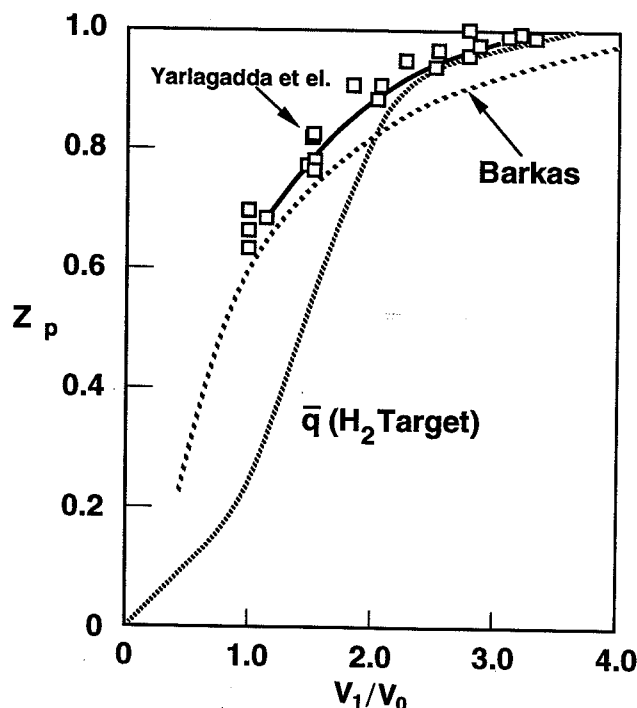


Fig. 4.25. The effective charge and equilibrium charge vs. velocity of protons in H_2 . \square and solid line, effective charge, $Z_{1\text{eff}}$ (Yarlagadda *et al.*, (1978); medium dashed line, effective charge, $Z_{1\text{eff}}$ (Barkas, 1963); short dashed line, average equilibrium charge, \bar{q} (Barnett *et al.*, 1977).

measurements presented by Barnett *et al.* (1977). If v_1 is the projectile velocity and v_0 is that of the bound electron, then for relative velocities greater than about $v_1/v_0 = 2.5$ (for protons, this corresponds to energies greater than about 100 keV), the equilibrium charge of the moving ion is essentially that of the bare nucleus and the two methods of arriving at an effective charge are equivalent. At lower proton energies, however, there are considerable differences among these methods of arriving at an effective charge. As discussed above, the effective charge for energy loss is generally larger than that based on the equilibrium charge obtained from charge transfer measurements.

4.7.5 Compilation of Experimental and Theoretical Work

Tables 4.6 to 4.8 summarize the experimental doubly differential cross section measurements that have been published on heavy ion impact. Neutral atomic hydrogen projectiles have also been included. In general, this tabulation excludes studies where only relative cross sections were reported.

For heavy ion impact, the projectile nuclear and ionic charges are important ionization parameters in addition to the impact energy and target. This requires a listing consisting of a four-dimensional matrix, making a rather complex catalog. Many studies were designed and performed to isolate and investi-

gate only specific ionization mechanisms; this means that collision systems, projectile charge states, and impact energies were chosen rather specifically and portions of, rather than the complete ionization spectra were often investigated. Thus, a complete range of all parameters is not usually available. The listing of available data, given in Tables 4.6 to 4.8, may be described as follows:

Targets studied: Roughly two thirds of the available data are for helium (representing simple) and argon (representing more complex) targets. Helium is often used as a target in many studies in order to minimize the effects of multiple ionization which can influence the interpretation of the experimental results and to simplify the theoretical modeling of these collisions. Molecular target studies are extremely rare.

Impact energies: Impact energies range from a few keV/u to many MeV/u. But for energies less than 0.5 MeV/u, typically only singly charged or neutral projectiles have been investigated; for more energetic collisions, highly charged projectile ions have been used.

Types of studies: These studies can be separated into several categories. For energetic, highly-charged heavy ion impact, TCEE and scaling effects have been studied. In this case, rather extensive angular and energy distribution information is available. For intermediate-energy collisions, heavy, dressed ions have been used to study abnormal effects in the binary encounter region. These data, therefore, generally exclude low-energy and large-angle electron emission. Intermediate-energy hydrogen and helium projectiles have been used to study projectile ionization and the dielectronic ionization mechanism. In this class of studies, the ejected electron energy and angular information is sometimes limited. At intermediate and low impact energies, various projectiles have been used to study the mono-electronic, dressed-ion mechanism, namely the partial screening of the projectile nuclear charge. Only H and He^+ projectiles have been investigated over a broad range of energies; the variation of the screening as a function of projectile ionic charge has been investigated at very few impact energies.

From a theoretical viewpoint, electron emission resulting from dressed-ion impact is very complex because projectile as well as target ionization plays a role and, in addition, both dielectronic and mono-electronic processes are important. Additional complications arise because the relative importance of multi-electron transitions, *e.g.*, multiple target, multiple projectile, and transfer ionization processes, increases for heavier-ion impact. Thus, many of the available theoretical treatments for dressed ion impact have only investigated specific ionization features, *e.g.*, electron loss from the projectile, BE electron emission, etc. Few treatments address the entire ionization spectrum.

TABLE 4.6—Published doubly differential cross sections for heavy projectile impact: low energies (1's to 10's ke-V)

Collision system	Impact energy (keV/u)	Secondary electron energy (eV)	Angles (degrees)	Source
H ₂ ⁺ -Ar	2.5-10	1-26	30-140	Sataka <i>et al.</i> (1979a)
He	1.25-4			
H ₂ ⁺ -Ar	2.5-10	2-26	30, 90	Sataka <i>et al.</i> (1979b)
He ⁺	1.25-5			
H ₂ ⁺ -He	2.5-10	2-50	30-120	Urakawa <i>et al.</i> (1981)
H ₃ ⁺	1.7-6.7			
H ₂ ⁺ -He	2.5-15	3-200	30-150	Tokoro and Oda (1985)
H ₃ ⁺	1.7-10			
He ⁺ -He	5	5-70	30-150	Tokoro <i>et al.</i> (1982)
H	15-150	1.5-300	10-160	Fryar <i>et al.</i> (1977)
H ₂ ⁺ -He	7.5-75			
³ He	5-50			
⁴ He	3.75-37.5			
H-He	15-150	1.5-300	15-150	Rudd <i>et al.</i> (1980)
H-H ₂ O	20-150	1-300	10-160	Bolorizadeh and Rudd (1986c)
He ²⁺ -He	60, 100	4-60	17	Irby <i>et al.</i> (1988)
He ²⁺ -He	50, 100	5-275	0-90	Bernardi <i>et al.</i> (1989)
He ²⁺ -He	50, 100	1-200	0-50	Bernardi <i>et al.</i> (1990)
Ne	100			
³ He ²⁺ -Ne	106	0.5-440	0-180	Suarez <i>et al.</i> (1993b)
He ²⁺ -He, Ne, Ar	50, 100	3-78	10, 20	Gay <i>et al.</i> (1990)
O ⁺ -Ar	3-31	5-500	16-160	Stolterfoht and Schneider (1979)
N ⁺	3.6-36			
Ne ⁺ -Ne	2.5-15	1.5-1000	10-160	Cacak and Jorgensen (1970)
Ne ^{q+} -Ne	1.25-40	1.6-1100	45-135	Woerlee <i>et al.</i> (1981)
q = 1-4				
Ar ⁺ -Ar	1.25-7.5	1.5-1000	10-160	Cacak and Jorgensen (1970)
Ar ⁺ -Ar	2.5	3-250	160	Rudd <i>et al.</i> (1966a)
Ar ²⁺ -Ar	17.5	100-500	90	Shanker <i>et al.</i> (1989)
Kr ^{q+} -Kr	0.3-8.5	16-1100	45-135	Gordeev <i>et al.</i> (1981)
q = 2-5				
Kr ^{q+} -Kr	0.6-12	80-1000	45-135	Gordeev <i>et al.</i> (1979)
q = 2-5				

For heavy bare-ion impact, experimental data have shown that the presence of two centers significantly alters the electron emission. Theories taking this into account are required since simple Z_1^2 scaling of proton impact cross sections obtained with hydrogenic wave functions are inadequate in many cases. Since much of the experimental work has concentrated on the investigation of deviations from scaled single-center mechanisms, comparison of particular experimental data sets with theory is not possible at this time.

Ion impact data can be evaluated according to the following criteria.

A) For bare ion impact, in regions where perturbation theories apply, the differential and TICSs should agree with scaled proton- or electron-impact cross sections.

B) For dressed-ion impact, the electron loss peak intensity should increase with the number of loosely

bound projectile electrons. Furthermore, the integrated peak intensity should agree with electron-impact differential elastic scattering cross sections and with total electron loss cross sections.

C) The integrated differential cross sections for electron emission must be in agreement with independently measured total cross sections.

D) For both bare- and dressed-ion impact on heavier targets, the target Auger emission from ns or np_{1/2} vacancies should be nearly isotropic as a function of laboratory emission angle and the integrated Auger intensities ought to agree with independent inner-shell ionization measurements.

E) Dressed-ion impact cross sections should scale quadratically with the mean equilibrium charge for low energy electron emission but approximately as Z_1^2 for high electron energies.

TABLE 4.7—Published doubly differential cross sections for heavy projectile impact: medium energies (100's keV/u)

Collision system	Impact energy (keV/u)	Secondary electron energy (eV)	Angles (degrees)	Source
He-Ar	100	8-80	0	Kuzel <i>et al.</i> (1993)
H-He	50-500	1-1500	15	DuBois and Manson (1993)
He ⁺² -He	50-250	1-300	15	DuBois (1993)
He ⁺ -Ar	75-500	1-4000	15-125	Toburen and Wilson (1979)
He ⁺²				
He ⁺ -H ₂ O	75-500	1-4000	15-125	Toburen <i>et al.</i> (1980)
He ⁺²				
H,He-He,Ar	200	10-400	0	Trabold <i>et al.</i> (1992)
He ⁺ -He,Ne, He ⁺² Ar	300	1-3500	15-125	Toburen and Wilson (1977a)
H ₂ ⁺ -H ₂	300-750	2-2000	20-125	Wilson and Toburen (1973)
H-He	500	10-500	90-150	Wang <i>et al.</i> (1992)
He ⁺				
H ₂ ⁺ -H ₂ ,HeHe	500, 1000	20-1000	30-140	Oda and Nishimura (1979)
He ⁺	250, 500			
H,He-He	500	20-1500	30	Heil <i>et al.</i> (1991)
He ⁺ -He	500	10-1300	20	DuBois and Manson (1986)
H-Ar	500	100-400	10, 170	Jakubassa (1980)
H-He,Ar	500	100-450	0-173	Hartley and Walters (1987)
He ⁺				
He ⁺ -He,Ne,Ar	500	10-700	95-170	Kövéř <i>et al.</i> (1988)
He ⁺ -He,Ne,Kr,H ₂ O, Ar	400-750	10-1500	20, 30 20-150	DuBois and Manson (1990)
H-He,Ar,Kr	500	20-1100	0-180	Kuzel (1991)
H ⁺	750	20-500	90	McKnight and Rains (1976)
H ₂ ⁺ -N ₂				
He ⁺				
He ⁺²				
H ₂ ⁺ -H ₂ ,He	800	50-2000	42	Kövéř <i>et al.</i> (1980)
He ⁺				
H ₂ ⁺ -Ar	800-2000	20-3000	0-60	Kövéř <i>et al.</i> (1982)
He ⁺				
H,He-He	500, 1000	20-1500	0-50	Heil <i>et al.</i> (1992)
C ⁺ -He,Ne,Ar,CH ₄	100	1-800	30, 90	Toburen (1979a)
C ⁺ -He	67-350	10-1500	15-130	Reinhold <i>et al.</i> (1990b)
C ⁺ -He	67-350	2-1500	15-130	Toburen <i>et al.</i> (1990b)
C ^{+q} -He	100	10-400	30	DuBois and Toburen (1991)
q = 0-3				
C ^{+q} -Ar	108-250	1-4000	15-130	Toburen (1979b)
q = 1-3				
O ^{+q} -H ₂ O	250	15-1100	15	Toburen (1991)
q = 1-3				
B ^{+q}	500	20-1500	10-60	DuBois <i>et al.</i> (1994)
C ^{+q} -He				
O ^{+q}				
F ^{+q}				
C ^{+q} -Ne,Ar				
q = 2-5, Q = 3-6				
I ⁺⁶ -H ₂ ,Ne	200-500	50-1500	17-60	Liao <i>et al.</i> (1992)
Cu ⁺³⁻⁵ -H ₂				
Au ⁺¹¹ -He				
Au ^{+q} -Ar				
q = 9, 11, 23				
Cu ⁺⁵ -He	530	70-2000	0	Jagutzki <i>et al.</i> (1991)
Cu ⁺¹⁵				
Au ⁺¹¹ -H ₂ ,He	600	50-1800	0-45	Wolf <i>et al.</i> (1993a)
I ⁺⁷	600	50-1800	0-50	Wolff <i>et al.</i> (1992)
I ⁺²³ -He,Ar				
Au ⁺¹¹				
Cu ⁺¹⁹	600	100-1800	0-50	Wolf <i>et al.</i> (1993b)
I ⁺²³ -Ar				
Au ⁺²⁹				

TABLE 4.8—Published doubly differential cross sections for heavy projectile impact: high energies (MeV/u)

Collision system	Impact energy (keV/u)	Secondary electron energy (eV)	Angles (degrees)	Source
H ⁺ C ⁺⁶ N ⁺⁷ -H ₂ , He O ⁺⁸ F ⁺⁹	1000, 2000	50-1500	0	Lee <i>et al.</i> (1990)
He ⁺² C ⁺⁶ -He O ⁺⁸	1000, 1840	4-2500	20-160	Pedersen <i>et al.</i> (1990, 91)
U ⁺³³ -Ne, Ar	1400	1-4000	20-90	Kelbch <i>et al.</i> (1989a,b)
O ^{+q} -O ₂ q = 4-8	1880	10-4000	25-90	Stolterfoht <i>et al.</i> (1974)
I ⁺²³ -He, Ar Xe ⁺²¹	600-3600	100-6000	17-60	Shinpaugh <i>et al.</i> (1993)
O ^{+q} -Ar q = 3-8	1060-2560	300-2000	90	Burch <i>et al.</i> (1973)
Xe ⁺²¹ -He, Ar	2400	100-6000	20	Wang <i>et al.</i> (1993)
Fe ^{+17,22} -He, Ar	3500	5-8000	27-155	Schneider <i>et al.</i> (1992)
C ⁺⁶ O ⁺⁸ -He, Ar Ne ⁺¹⁰	5000	2-5000	20-160	Platten (1986) Platten <i>et al.</i> (1987)
U ⁺³⁸ -He, Ar Th ⁺³⁸	6000	5-5000	20-150	Schneider <i>et al.</i> (1989)
Mo ⁺⁴⁰ -He	25000	2-5000	20-160	Stolterfoht <i>et al.</i> (1987)